学位論文

Development of linear and nonlinear microspectroscopy for nondestructive redox state analysis of hemoproteins in biological samples

（ 非破壊に生体内ヘムタンパク質の酸化還元状態を分析する

線形・非線形顕微分光法の開発 ）

平成２７年１２月博士（理学）申請

東京大学大学院理学系研究科

化学専攻

瀬川　尋貴

Development of linear and nonlinear microspectroscopy for nondestructive redox state analysis of hemoproteins in biological samples

A thesis submitted to the University of Tokyo
for the degree of doctor of Science
[Hakushi (Rigaku)]

Hiroki SEGAWA

Department of Chemistry, School of Science
the University of Tokyo

December, 2015

Table of Contents

Abstract

Redox state of biomolecules is strictly controlled by a mechanism of homeostasis. In the native state, redox equilibrium of the redox active molecules plays a key role to maintain the health of life body. For example, an excess amount of oxidant such as reactive oxygen species (ROS) induces cellular death process because the oxidative stress damages lipids, proteins and nucleic acids. There have been many studies that report the relations between ROS and human disease or aging. On the other hand, redox equilibrium is used for signal transduction like protein-protein interactions and gene expressions. But the underlying detailed molecular mechanisms are not clear yet.

Hemoproteins are one of the redox active proteins and function to eliminate the toxic chemicals, produce energy and so on. Previously, many studies have analyzed the relation between the redox state of hemoproteins such as cytochrome species and hemoglobin, and their functional mechanism. Many studies used *in vitro* or destructive experiments including the extraction of cellular components and homogenization. The destructive experiment is, however, inappropriate for the analysis of the redox state because the ambient oxygen can oxidize the samples and it is impossible to analyze the redox state of the molecule inside the life body. The simplest way to overcome this problem is directly analyzing the redox state of molecules inside living cells. In this thesis study, I developed two microspectroscpic methods which enabled quantification and qualification of the hemoproteins in a nondestructive manner.

One is based on resonance Raman scattering. Hemoproteins possess two major absorption bands, namely Soret band (around 410 nm) and Q-band (around 550 nm). Some previous studies have reported the application of 532 nm excitation (Q-band resonance) Raman scattering to quantify the redox state of the intracellular cytochrome species. In this thesis, I developed a 405 nm excitation (Soret band resonance) Raman microspetroscopy to increase the sensitivity and precision. By the developed setup and the spectral fitting technique, quantification of the each oxidized and reduced intracellular cytochrome was achieved.

Quantitative evaluation of experimental precision of 405 nm and 532 nm excitation was performed. At last, I applied the developed method to trace the dynamic behavior of the intracellular redox state of cytochromes during UV-stimuli triggered apoptosis.

The other is a novel spectroscopic technique, electronically resonant multiplex third-order sum frequency generation (TSFG). TSFG is a non-degenerate analogue of third harmonic generation (THG). In this study, I confirmed the electronic resonance enhancement of TSFG signals from cytochrome and hemoglobin. The observed TSFG was resonant with Soret band transition, which altered its absorption spectra depending on the redox state of hemoproteins. I theoretically revealed the interpretation of resonance TSFG spectroscopy, and found the possibility of direct extraction of the information on the electronic state of hemoproteins from the spectral analysis of resonance TSFG spectra.

At last, I discuss the applicability of the developed system to bioimaging. By the application of the developed microscopic system, the inner structure of the rat cornea was visualized based on the contrast mechanism of TSFG and the other observed nonlinear optical processes.

Table of abbreviations

Abbreviation	Description
ASF	amplitude spread function
BSA	bovine serum albumin
CARS	coherent anti-Stokes Raman scattering
CTF	coherent transfer function
CYP	cytochrome P450
cyt b	cytochrome b
cyt c	cytochrome c
Ep	corneal epithelium
FWHM	full width of half maximum
Hb	hemoglobin
MEM	maximum entropy method
PBS	phosphate buffered saline
ROS	reactive oxygen species
RRS	resonance Raman scattering
SHG	second harmonic generation
St	corneal stroma
THG	third harmonic generation
TSFG	third-order sum frequency generation

Chapter 1

General Introduction

1.1. Hemoproteins and redox reaction in the native state of life

Intracellular redox state is strictly controlled by a mechanism of homeostasis. In the native state, redox equilibrium of intracellular molecules plays a key role to maintain the life of cells. An excess amount of oxidant such as reactive oxygen species (ROS) induces the cellular death processes because the oxidative stress damages many biomolecules such as proteins, nucleic acids and lipids[1–5]. Relations between ROS and various human disease and aging have also been reported[6–8]. On the other hand, the signal transduction processes such as protein-protein interactions and gene expression use the redox reaction as a signaling factor. However, the molecular mechanism underlying the intracellular signaling through the redox reaction is still unclear.

Hemoproteins are one of the redox active proteins in life body. All hemoproteins contain the co-factor called heme, which consists of porphyrin ring with the Fe ion at the center. The representative chemical structure of heme is depicted in Fig. 1-1. There a few types of heme called heme a, heme b, heme c and so on. The difference of each heme type is the functional group attached to the pyrrole ring. Through the covalent and non-covalent interaction between the functional group, the center iron and the amino acid residue of the apoprotein, the structure of the hemoprotein is constructed. By changing the charge state of Fe ion in response to the surrounding environment, hemoproteins can alter its redox state. Although the amino acid sequence and the higher order structure of hemoproteins vary, heme is the common character of the all hemoproteins[9].

Many functions of hemoproteins are attained by the redox labile heme group. For example, mitochondrial hemoproteins cytochrome *b* (cyt b) possessing heme b and cytochrome *c* (cyt c) possessing heme c are indispensable components of the electron transportation chain (or oxidative phosphorylation), which is one of the energy production systems of mammalian cells[10]. In this energy production system, cyt b and cyt c make a complex in the inner mitochondrial membrane, and transport an electron to the free cyt c in the intermembrane space

of mitochondria[10]. All transportation processes of the electron were performed through redox reaction. Since the electron transportation chain is the major process of the ATP synthesis from fatty acid, the deficiency to this system induces serious disorder called mitochondrial disease[11,12]. Another example is cytochrome P450 (CYP). CYP is the general term of the families of hemoproteins with heme b which function as enzymes for the oxidation of various substances[13]. Many types of drugs are metabolized through the reaction with CYP. Although cyt b and cyt c locate in mitochondria, CYP is contained mainly in microsomes. As indicated here, hemoproteins contain cofactor heme as a common structure. But the functions taken in life body are various in hemoproteins.

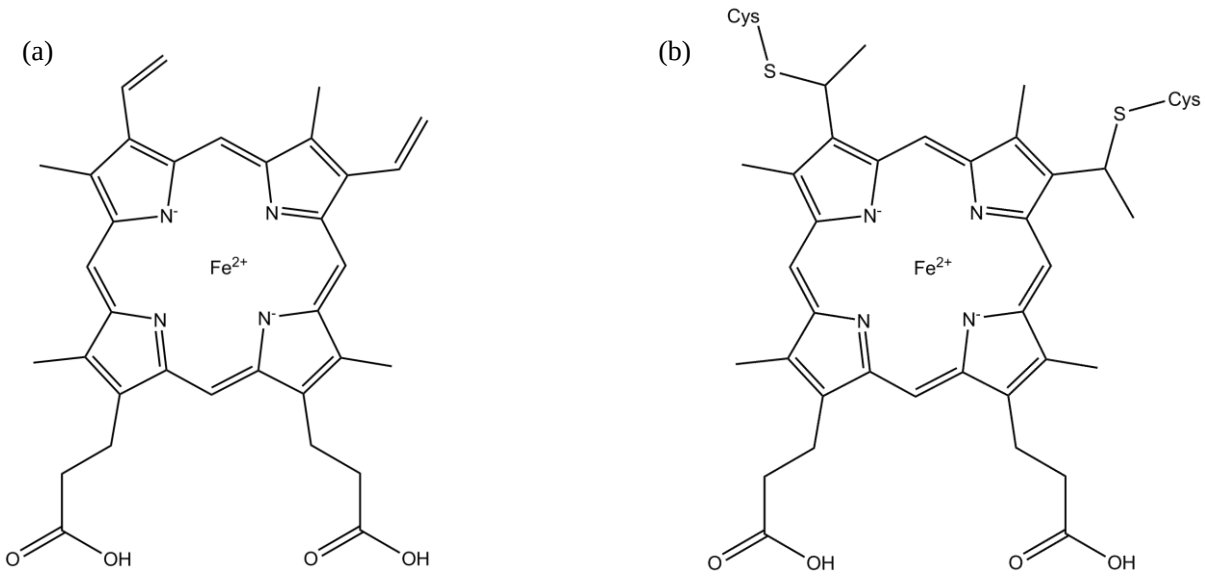

Fig. 1-1 Chemical structure of (a) heme b and (b) heme c of the reduced form.

1.2. Relation between cytochromes and apoptosis

In the native state of cells, cyt b and cyt c are necessary for energy production as described in the previous section. On the other hand, cyt c is also known as a critical signaling protein in apoptotic signal transduction system[4,14–19].

Apoptosis is one of the cellular death processes, frequently called programed cell death. The main functions of apoptosis are (i) the formation of our bodies at the developmental stage, and (ii) the removal of damaged cells which possibly become a reason of tumor and other disorders[20–22]. On the contrary to necrosis (called traumatic cell death), apoptosis is thus indispensable to maintain the health of life bodies.

At the initiation step of apoptotic signal transduction process, cyt c is released from mitochondria to cellular cytoplasm in mammalian cells. Apoptotic protease activating factor 1 (Apaf-1) in the cytoplasm interacts with the released cyt c, and constructs a huge protein complex named apoptosome. This complex behaves as a hub of apoptotic signal transduction, and activates the executor protease, caspase[3,18]. Once caspase is activated, the apoptotic process acceleratedly proceeds and results in nuclear condensation, DNA fragmentation, protein degradation and cell structural change. Therefore investigating the dynamics of cyt c in living cells is important for correct understanding of apoptotic signal transduction process. In fact, many previous studies have analyzed the behavior of cyt c and other signaling molecules during apoptosis[22–24].

1.3. Relation between redox state of cytochromes and apoptosis

To date, many previous studies have analyzed the relation between the redox state of cyt c and the apoptotic signal transduction process[2–4,19,25,26]. The point of the discussion is whether both oxidized and reduced cyt c can equally proceed the apoptosis. In the early studies, Hampton et al. reported that cyt c added to the extract of the cellular cytoplasm was rapidly reduced[19]. Thus they concluded that the redox state of cyt c was irrelevant to the apoptotic process because the released cyt c would be reduced in the cytoplasm. Kluck et al. reported that the oxidation of cyt c by the addition of potassium ferricyanide to the extract of the cytoplasm inhibited the caspase activation[27]. However, caspase itself could be inactivated by oxidation, thus it was unclear whether both oxidized and reduced cyt c could proceed apoptosis.

Lately, other studies have found that the ability of apoptotic signal transduction of cyt c might depend on its redox state. Some researchers reported that the addition of oxidized cyt c to the cell extract showed apoptotic activity, but the addition of reduced forms did not[26]. The activation by the oxidized cyt c was inhibited by the addition of reductant such as glutathione and ascorbate[28]. Moreover, if the reduced cyt c and cytochrome c oxidase, which could specifically oxidize cyt c, were simultaneously added to the cell extract, the activation of caspase was induced[4]. These results indicated that the ability of apoptotic signal transduction of each oxidized and reduced cyt c was not equal.

However, the experimental procedures used in the previous studies were in vitro, or destructive techniques including the extraction of cellular components. Since the ambient atmosphere is capable of oxidizing the samples due to oxygen molecules, the destructive experiment was inappropriate to observe the redox state. Moreover, above mentioned experiments were unable to discuss the redox state of cytochromes inside the apoptotic cells.

1.4. Hemoglobin and its redox state

Hemoglobin (Hb) is another example of redox active hemoproteins and is also indispensable to maintain our life. Hb is a major component of erythrocytes in blood, and is a transporter of the oxygen molecules. In the native state, Hb is kept in the reduced form because only the reduced form of Hb is able to transport the oxygen molecules[29]. By the equilibrium of Hb-O_2 interaction, Hb releases the oxygen molecule when the concentration of the oxygen in the surrounding environment is decreased. The difference of the ability of the oxygen transportation between the reduced and the oxidized forms is originated from the difference of the affinity of Hb-O_2 interaction. In general, reduced Hb possesses higher affinity than the oxidized form (called methemoglobin). This tendency of the affinity is the same in the case of other gas molecules including toxic gasses such as carbon monoxide and dihydrogen sulfate[30,31]. Thus forced oxidation of Hb is sometimes used for the purpose of therapeutic (detoxification)[31].

If the occupancy of the oxidized form of Hb increases, the circulation of oxygen is disturbed and it will lead into sever disorders. The symptom of excess increase of the oxidized Hb is called methemoglobinemia[32]. In order to investigate the reason of this disorder, understanding the molecular mechanism of redox equilibrium of Hb in the life body without destructive experimental processes is of great importance.

1.5. Purpose and contents of this thesis study

As mentioned in the previous sections, nondestructive analytical methods for hemoprotein's redox state in biological samples are indispensable to investigate the relation between the molecular redox state and biological functions. Spectroscopy is one of the promising methods because it uses light, which is one of the low invasive perturbations, and obtained spectra provide structural and quantitative information on the target molecules. In this thesis, I tried to develop two types of spectroscopic analytical techniques for nondestructive redox state analysis.

The first one is 405 nm excitation resonance Raman scattering (RRS). Similar to (nonresonant) Raman scattering, the intensity of RRS signal is strictly proportional to the number of molecules. Thus RRS would enable nondestructive analysis in a quantitative manner. By using the resonant enhancement of the signals from cytochrome species, μM-scale intracellular cytochrome species can be specifically identified among the vast amounts of other biomolecuels. I compared the developed method with the previously reported 532 nm excitation scheme, and applied it to monitor the redox dynamics of cyt b and cyt c during apoptosis.

The second one is electronically resonant third-order sum frequency generation. Third-order sum frequency generation (TSFG) is an analogue of third harmonic generation (THG). The difference between the two processes is the number of wavelength used for signal generation. By the combination of multiplex scheme and resonance effect of TSFG, resonant TSFG spectrum is obtainable. I found that Spectral analysis of resonant TSFG spectra could provide the information on the redox state of Hb.

At last, I introduce the attempt to apply the developed TSFG microspectroscopy to the imaging of rat corneal tissue. In this section, it is revealed that TSFG is applicable to the biological imaging. Although the spectral information of TSFG was not fully used, significant information on the structure of the sample still could be extracted from TSFG images.

Chapter 2

405 nm excitation resonance Raman microspectroscopy

2.1. Introduction

Raman spectroscopy is a kind of vibrational spectroscopy based on Raman scattering[33,34]. If the incident light is irradiated to a molecule, inelastic scattered light (Raman scattering) can be found in the vast amount of elastic scattered light (Rayleigh scattering). The resulted wavelength of the inelastic scattered light (ω_{Raman}) is $\omega_1 + \Omega$ or $\omega_1 - \Omega$, where ω_1 is the wavenumber of the incident light and Ω is that of the difference between ω_1 and ω_{Raman}. The light with the wavenumber of $\omega_1 + \Omega$ is called anti-Stoles Raman scattering, and with $\omega_1 - \Omega$ is called Stokes Raman scattering. The difference of wavenumber (Ω) between the incident light and the inelastic scattered light corresponds to the wavenumber of the molecular vibration of the irradiated molecule. Therefore, the typical spectrum of the Raman scattering can be illustrated as Fig. 2-1a. The Raman spectrum contains the information on the molecular vibration. This is an abstract of Raman scattering. In general, the intensity of anti-Stokes Raman scattering is weaker than that of Stokes Raman scattering. Thus the signal of Stokes Raman scattering is normally used for spectral analysis. Since the molecular vibration is deeply related to the molecular chemical structure, Raman spectroscopy provides the plenty molecular structural information[35]. Therefore Raman spectra are frequently called molecular fingerprinting. In addition to this, the intensity of signals of Raman scattering is strictly proportional to the number of molecules. Due to its quantitative character and low invasiveness, Raman scattering has been frequently applied to the biological studies[36–42].

In the mechanism of Raman scattering, so-called virtual state is related. The schematic energy diagram of nonresonant Raman scattering is frequently described as Fig. 2-1b. In this figure, $|g\rangle$ corresponds to the ground electronic state and $|e\rangle$ corresponds to the virtual state of a molecule. In the nonresonant condition, the energy of $|e\rangle$ is far from the excited electronic state of the molecule. On the other hand, if the energy of the incident light and that of the electronic transition of a molecule is close to each other, the signal of Raman scattering is resonantly enhanced through the interaction with the vibronic state of the molecule. This

phenomenon is called resonance Raman scattering (RRS) (Fig. 2-1b)[43,44]. Due to the resonance enhancement, the intensity of the signal of RRS is more than 10^3 folds larger in comparison to that of nonresonant Raman scattering. Thus, by using RRS, we are able to identify the small concentration molecules in the vast variety of dense molecules in living cells[45].

It is well known that hemoproteins including cytochrome species possess two major absorption bands in the visible wavelength region, namely Soret band around 410 nm and Q-band around 550 nm (see the absorption spectrum of cyt c shown in Fig. 2-2)[46,47]. By tuning the excitation wavelength to these absorption regions, RRS from cytochrome species can be observed. In fact, some previous studies attempted to quantify the intracellular cytochrome species by using 532 nm RRS resonant with Q-band[45,48,49]. In 532 nm excitation scheme, however, the intensity of the oxidized form was apparently quite weaker than that of the reduced form. Thus the experimental precision of quantifying the oxidized form was inferred to be bad.

As shown in the absorption spectra (Fig. 2-2), the absorption coefficient of Soret band is 5 times larger than that of Q-band. This fact indicates that RRS resonant with Soret band is expected to provide stronger signals than 532 nm excitation RRS resonant with Q-band provides. In this chapter, I chose 405 nm excitation system to improve the intensity of RRS signals and applied the developed new RRS scheme to quantify the intracellular redox state of cytochrome species.

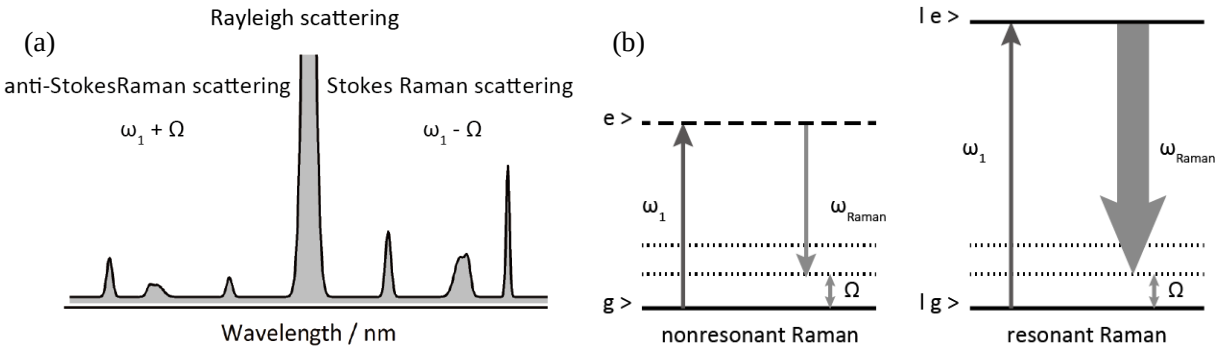

Fig. 2-1 Schematic of the Raman spectroscopy and Raman scattering. (a) An example of the experimentally obtainable Raman spectrum. (b) Schematic energy diagrams of Raman scattering of nonresonant and resonant conditions. The black line means the vibronic state of the molecule, the dotted line means the vibrational state, and the broken line means the virtual state.

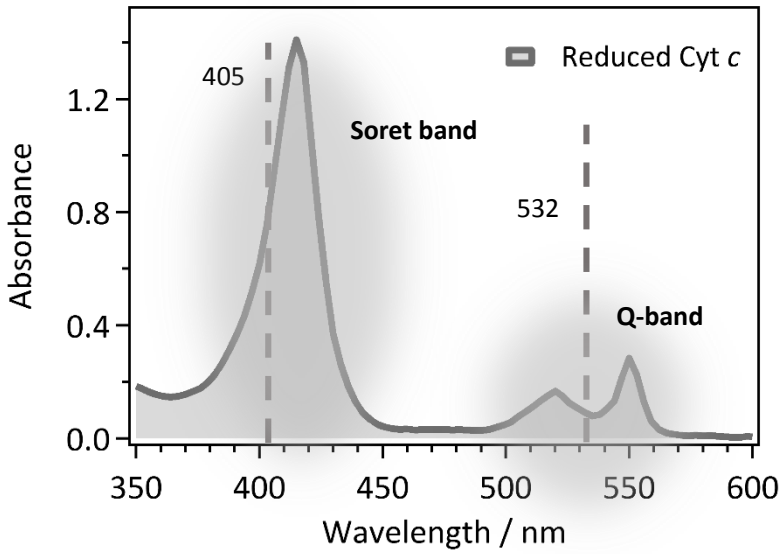

Fig. 2-2 Absorption spectrum of cytochrome c solution (reduced form). The absorption bands of Soret band (around 410 nm) and Q-band (around 550 nm) are indicated for clarity. The broken line means the wavelength of 405 nm and 532 nm which were used for RRS measurement.

2.2. Experimental

2.2.1. Optical system

The developed RRS microscope is depicted in Fig. 2-3. This system possesses two excitation laser lines to compare 405 nm excitation and 532 nm excitation under the same experimental condition. The light source of 405 nm system was a wavelength stabilized diode laser (SureLock LM, ONDAX). After the expansion of irradiation diameter and the rotation of polarization, 405 nm light was introduced into an inverted microscope (IX71, Olympus), and irradiated onto a sample through an objective lens (x60, 1.25 NA, Oil immersion, Olympus). The samples was placed upon a piezo electric stage (P-527 3CD, PI Japan). The typical laser power at the sample point was 2.3 mW. The back scattered Raman signals were collected by the same objective lens and passed through a beam splitter with transmittance/reflectance = 9/1 property. Then the signal passed a confocal pinhole with 75 μm in diameter and was introduced into a spectrograph (iHR320, HORIBA) after removing the excitation light by long-pass filters. An EMCCD camera (iXon Ultra 897, Andor) was used for detection of the signal. In the case of 532 nm excitation scheme, some components were exchanged. The light source was a frequency-doubled cw Nd:YVO_4 laser (Millennia Pro, Spectra Physics). Elimination of the excitation light was performed by a notch filter, and the detection camera was changed to a liquid-nitrogen cooled CCD camera (Spec-X, Princeton Instruments).

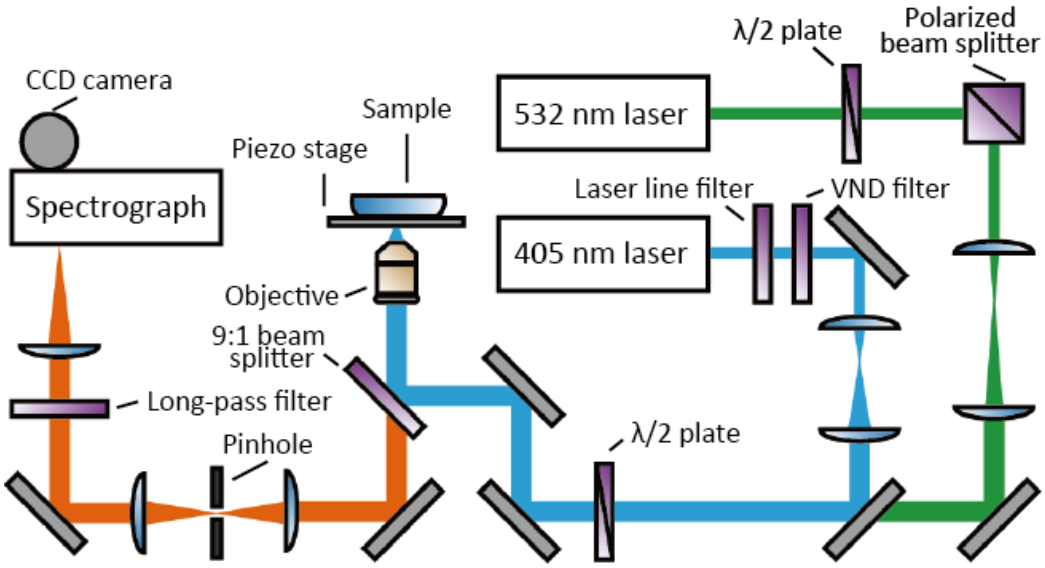

Fig. 2-3 Schematic diagram of the developed 405 nm excitation resonance Raman spectral microscope.

2.2.2. Sample preparation and measurement

Standard cytochrome solutions

The dry powder cyt c (cyt c from Bovine Serum, Sigma Aldrich Japan) was dissolved in phosphate buffered saline (PBS). To completely control the redox state of cyt c solution, I added an excess amount of sodium ascorbate as a reductant, and potassium ferricyanide as an oxidant. The redox state of the solution was confirmed by the absorption spectra as shown in Fig. 2-4 which were consistent with spectra shown in the previous studies[28,50]. The concentration of cyt c solution was estimated from the absorption coefficient described on the previous study[51]. In the case of cyt b, the sample was provided as diluted PBS solution (cytochrome b_5 human recombinant, Sigma Aldrich Japan). Since the total volume of the solution was not so large, I prepared dense sodium ascorbate solution (reductant) and potassium ferricyanide solution (oxidant) in order to regulate the redox state of cyt b. The mixture of cyt b solution and reductant/oxidant were used as the standard solution. Redox state of cyt b standard was checked by absorption spectra as shown in Fig. 2-4 which were consistent with the previous studies[52]. The concentration of standard cyt b solutions was calculated from the differential absorption coefficient provided by Sigma Aldrich Japan.

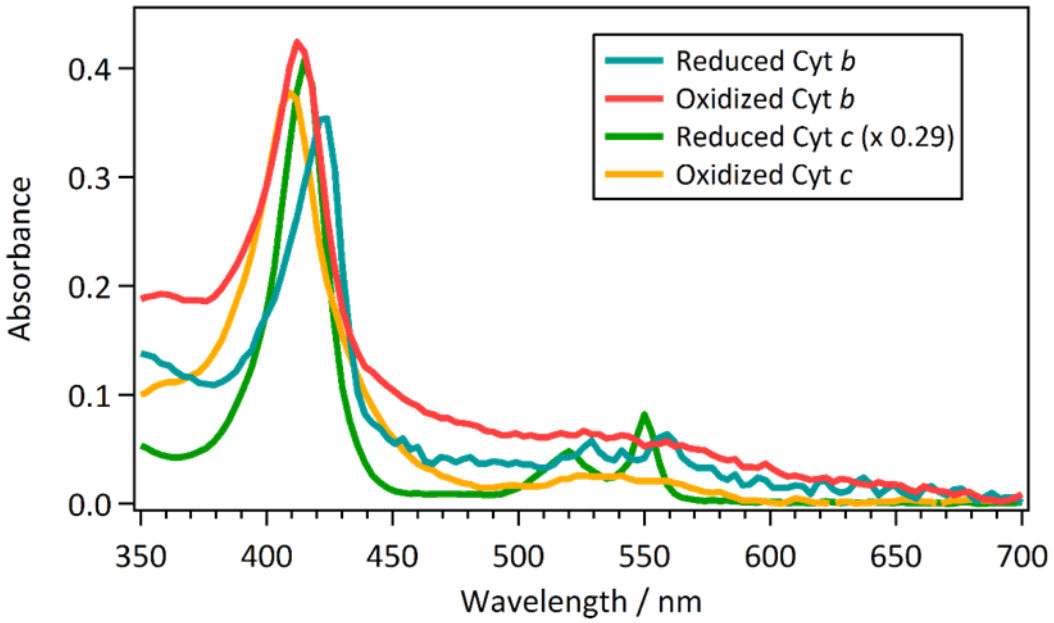

Fig. 2-4 Absorption spectra of standard cytochrome solutions.

Measurement and analysis of standard Raman spectra of cytochrome species

After the confirmation of the redox state of the prepared cytochrome solutions, I dropped the solutions onto glass-bottom dishes. In order to prevent evaporation of the solution, the Raman spectra of the each cytochrome species were quickly measured. In the observation, raster scanning of the liquid samples was performed in order to avoid the intensity fluctuation originated from various optical effect such as photobleaching and thermal lens effect of cytochromes.

The obtained standard Raman spectra passed through data processing. After subtraction of the dark noise, the wavelength dependence of the sensitivity of the detector was normalized by using the signal from halogen lamp. The background signals of solvent and reductant/oxidant were subtracted by using their spectra. Broad fluorescence signal was eliminated by polynomial fitting technique[53]. The four standard spectra, namely reduced cyt b, oxidized cyt b, reduced cyt c and oxidized cyt c, were normalized to the same concentration and experimental condition.

Cell culture

All cellular samples measured in this study were the wild type HeLa cell. Cells were cultured on 35 mm glass-base dish (Iwaki) for Raman measurement, and on 6-well plate (Nunc) for viability assay. The culture medium was Dulbecco's Modified Eagle's Medium (DMEM) high-glucose with L-glutamine, phenol red, fetal bovine serum (FBS) and penicillin-streptomycin (Pen Strep). The culture dish was incubated in a CO_2 incubator with 5 % concentration, 37 degree Celsius.

Cell viability assay

The cell viability was measured by trypan blue assay following the protocol offered by the manufacture. Before apoptotic stimulation, the culture medium was changed to the imaging buffer (DMEM high-glucose with L-glutamine and without phenol red, FBS and Pen Strep). This manipulation is indispensable because ultraviolet (UV) light was absorbed by the additives. At time zero, UV-C light (10 mJ/cm^2) was irradiated onto HeLa cells cultured on 6-well plates. The irradiated cells were then incubated in the CO_2 incubator with 5 % concentration, 37 degree Celsius. At some point in time, 3 dishes in 6-well plates were supplied to viability assay (Fig. 2-5). The culture medium was transferred to micro test tubes and the dish was washed out by PBS three times. Then trypsin solution was added to the dish and incubated in the CO_2 incubator with 5 % concentration, 37 degree Celsius, for 1 minute. Then the suspension with cells was transferred into the micro test tube and centrifuged. Supernatant was removed and then the precipitated cells were re-suspended by the mixture of PBS and trypan blue 0.4 % (w/v) solution with the same volume. Then the tube was incubated in room temperature for 1 minute, and the numbers of stained and unstained cells were counted by an automated cell counter Countess (Life Technologies). In this case, unstained cells were regarded as being live and stained cells were regarded as being dead.

Measurement and analysis of Raman spectra from HeLa cells

Before Raman measurement, the culture medium was changed to the imaging buffer. To achieve high signal-to-noise ratio measurement of HeLa cells, spatially averaging method was adopted (see Fig. 2-6). The CCD camera and the stage were simultaneously triggered at the start of measurement. Generated signals from each scanning point were accumulated on limited numbers of frames of the CCD camera. Thus the obtained signal corresponded to the summation (or average) over the whole single cell area.

On the apoptosis experiment, several different single HeLa cells on the single dish were measured. Several dishes were prepared on each experimental day. Culture medium was changed to the imaging buffer described in the previous section before apoptosis stimulation. Then all dishes (except for the negative control) were simultaneously irradiated by UV-C light (10 mJ/cm^2) and incubated in a CO_2 incubator with 5 % concentration, 37 degree Celsius. The time course of the experiment was the same as that of the cell viability assay (Fig. 2-5). At each time point, one dish was immediately placed upon the microscope stage and RRS measurement was performed.

Spectral fitting

Quantification of the redox state of intracellular cytochrome species was performed through spectral fitting technique. This method is frequently called classical least square regression, direct classical least square or biomolecular component analysis[54–57]. In this analysis, the experimentally obtained spectra were decomposed into linear combination of the standard Raman spectra of constituent molecules of the object (Fig. 2-7) through least squares method or matrix operation. Since the intensity of the Raman scattering is proportional to the number of molecules, the fitting coefficients can be quantitatively evaluated.

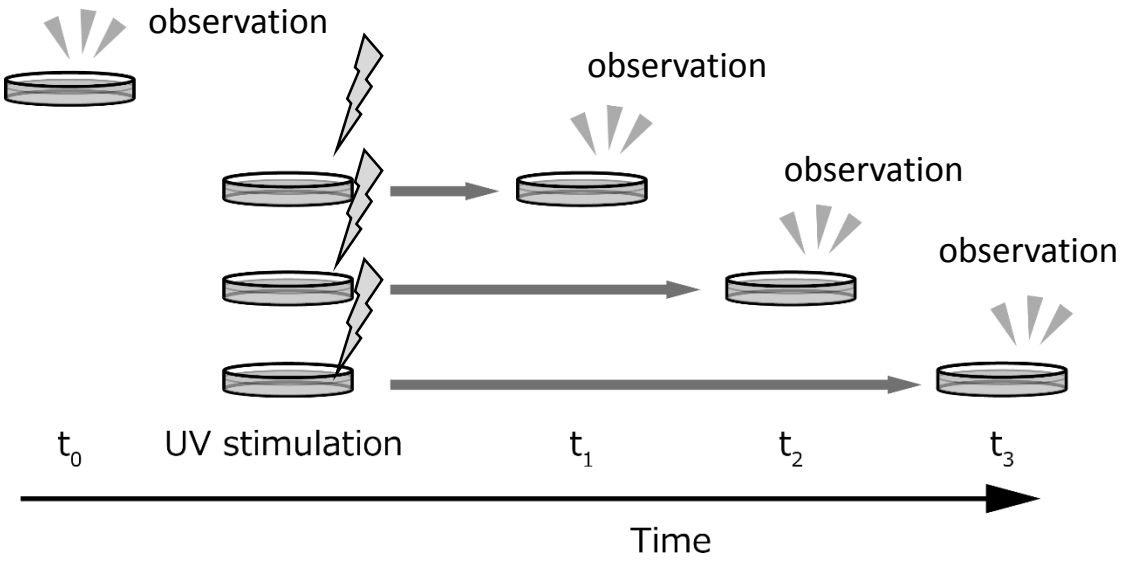

Fig. 2-5 Experimental scheme of apoptotic cell measurement. Before stimulation, the medium filling the dish was changed to the imaging buffer. And then UV irradiation was applied at the time zero except for the control experiment. At each time point, one dish was supplied to the measurement.

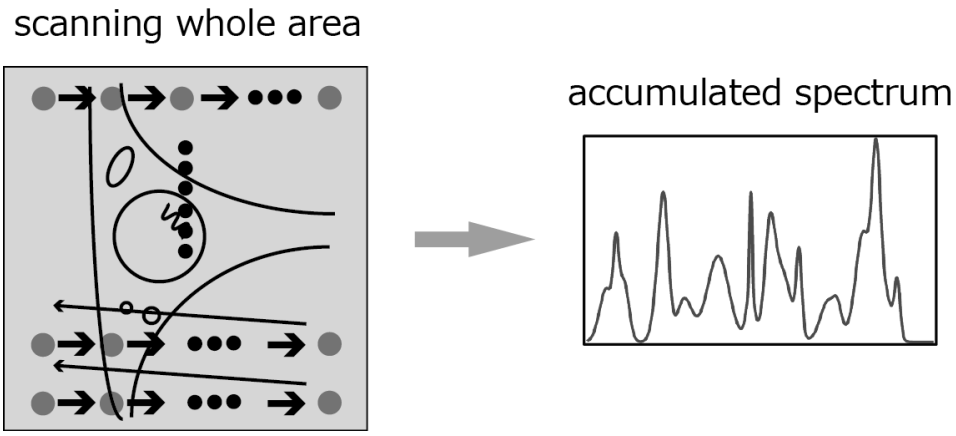

Fig. 2-6 Experimental schematic of the spatial averaging measurement of Raman spectra from HeLa cells. After the simultaneous triggering of the sample stage and the CCD camera, raster scanning was started. The generated signals were collected into the small limited numbers of frames of the CCD camera. Thus the obtained accumulated spectrum did not contain the spatial information.

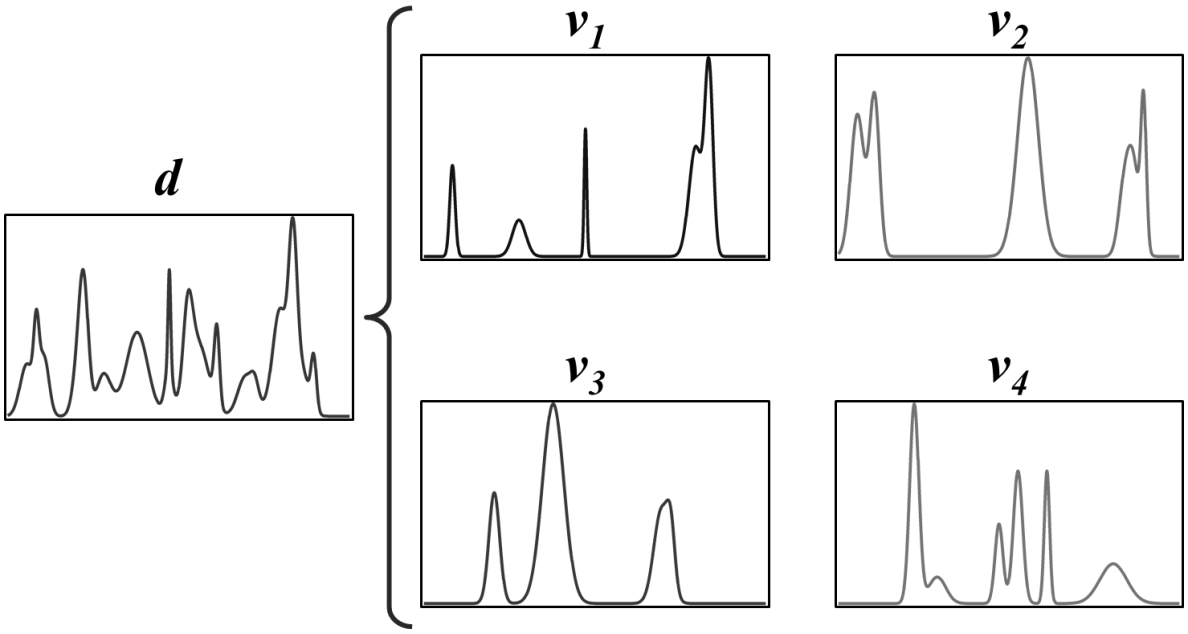

$$d = \alpha\, v_1 + \beta\, v_2 + \gamma\, v_3 + \delta\, v_4$$

Fig. 2-7 The schematic of spectral fitting analysis. The experimentally obtained spectrum (*d*) was decomposed into linear combination of the standard spectra of the known constituent molecules (v_1, v_2, v_3, v_4, in this figure). The fitting coefficients (α, β, γ, δ, in this figure) was determined through the least square method and matrix operation.

2.3. Standard Raman spectra of cytochrome species

Observed standard Raman spectra of reduced and oxidized forms of each cyt b and cyt c by 405 nm excitation are shown in Fig. 2-8. All four spectra showed the characteristic bands originated from cytochrome species such as around 1360 cm^{-1} (porphyrin skeletal vibration) and 700 cm^{-1} (pyrrole ring vibration)[47]. On the other hand, the detailed peak position, band width and the ratio of band intensities were unique for each species. These differences were originated from the chemical structure of each heme type and the electronic state (or the absorption). The chemical structure difference changes the peak position of the Raman band, and the electronic state difference changes the factor of the resonance enhancement for each Raman band. This indicated that the obtained standard Raman spectra could be used to identify each cytochrome species from the experimentally obtained spectra.

Raman spectra of four standard cytochrome solutions by 532 nm excitation were also observed. The obtained result is shown in Fig. 2-9. All four spectra showed the characteristic bands originated from cytochrome species such as around 1130 cm^{-1} (porphyrin CH vibration) and 750 cm^{-1} (pyrrole ring vibration)[47]. These spectra were normalized to the same concentration and experimental condition as that 405 nm excitation spectra were observed. All four spectra provided the consistent spectral patterns with the previously reported spectra[47,52].

To compare the experimental precision of 405 nm excitation and 532 nm excitation, I evaluated the contribution from the spectral intensity and similarity. First, the ratio (reduced cyt b : oxidized cyt b : reduced cyt c : oxidized cyt c) of the calculated integral intensity of four standard Raman spectra of cytochromes is 1.0 : 0.70 : 0.64 : 0.38 for 405 nm excitation. On the other hand, the ratio is 1.0 : 0.28 : 0.67 : 0.048 for 532 nm excitation. In addition, the ratio of the integral intensity of the 405 nm and 532 nm excitation schemes became comparable after normalization of the spectral intensity based on the intensity of the Raman band of the external standard (here the band around 1020 cm^{-1} of indene was used). Calculated ratio is summarized in the Table 2-1. As it is clear, the difference of the intensity between reduced and oxidized

forms is more than 10 folds in the case of 532 nm excitation. In the 405 nm excitation, the difference of the intensity is 2.5 folds and quite smaller than 532 nm. In addition, all four standard spectra obtained by 405 nm excitation provided stronger signals than 532 nm excitation. The difference of the intensity of signals between 405 nm and 532 nm was reasonable because the absorption coefficient (see Fig. 2-2 and 2-4) of Soret band is larger than that of Q-band and thus the stronger enhancement could be expected in 405 nm than in 532 nm. This result indicates that the expected experimental precision of quantifying the redox state by 405 nm excitation is better than that by 532 nm excitation.

Next, the effect of spectral similarity was considered. If the standard spectra were similar to each other, it was inferred that the fitting precision of spectral fitting technique would get worse. In order to consider the contribution from spectral similarity, synthesized spectra with the same signal-to-noise ratio by adding four standard Raman spectra of cytochromes and small random noise were constructed in both 405 nm and 532 nm cases (Fig. 2-10). Then spectral fitting analysis was applied to the synthesized spectra by using four cytochrome standard spectra as the basis set. The averaged relative errors of the four fitting coefficients is 4 % for 405 nm excitation and 1 % for 532 nm excitation. Therefore, from the view point of spectral similarity, 532 nm excitation provided better fitting errors.

The result of spectral intensity and similarity showed the opposite conclusion. Namely, from the view point of spectral intensity, 405 nm excitation scheme was expected to be better than 532 nm excitation scheme. On the other hand, from the view point of spectral similarity, 532 nm excitation scheme was better than 405 nm excitation. Under the current experimental condition, the difference between the two excitation schemes in the intensity was, however, estimated more significant than that in the similarity because the amount of intracellular cytochrome was inferred to be small as μM scale. If the concentration of the intracellular cytochromes is large and the spectra with extremely high signal-to-noise ratio are obtainable, 532 nm excitation is inferred to provide the better experimental result than 405 nm excitation.

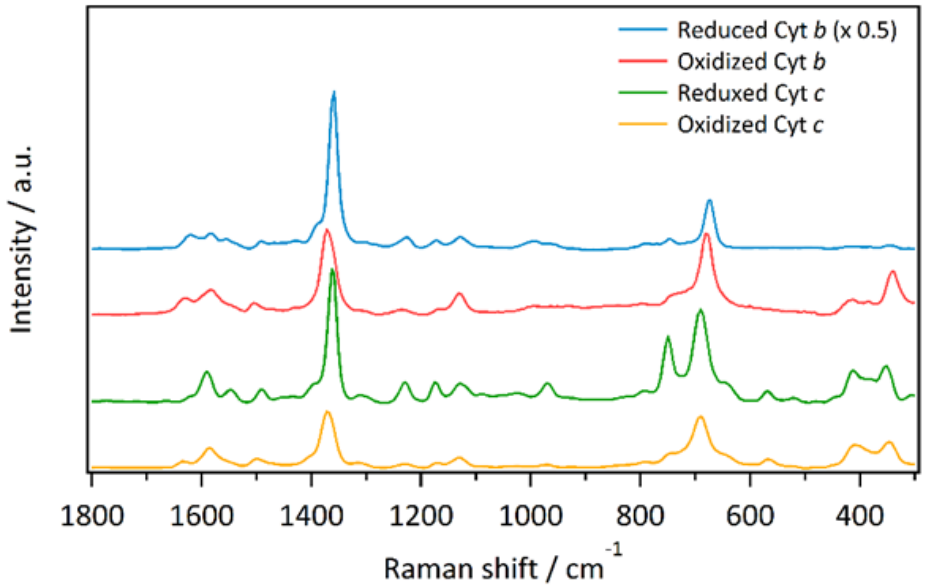

Fig. 2-8 Observed Raman spectra of standard cytochrome solutions by 405 nm excitation.

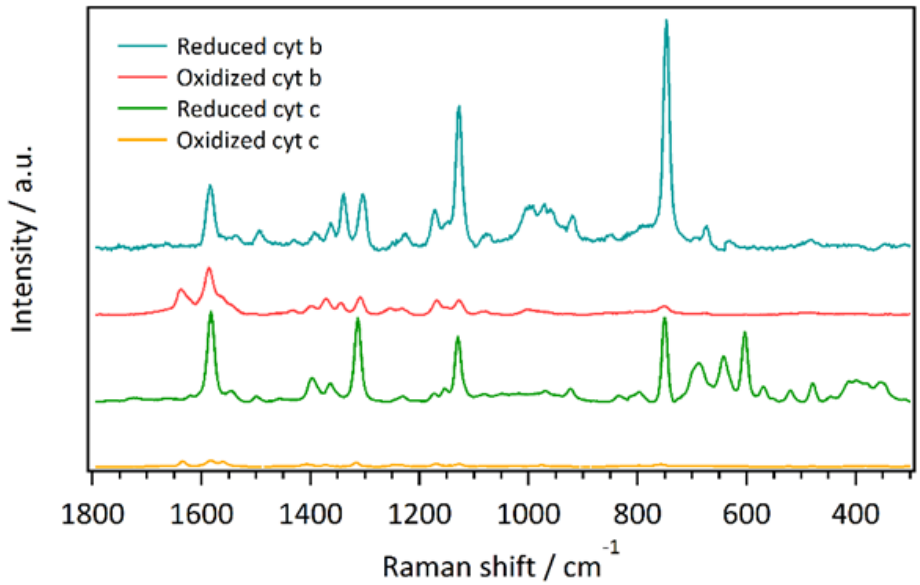

Fig. 2-9 Observed Raman spectra of standard cytochrome solutions by 532 nm excitation.

Table 2-1 Calculated ratio of the integral intensity of four standard Raman spectra of cytochromes.

	reduced cyt b	oxidized cyt b	reduced cyt c	oxidized cyt c
405 nm	1	0.7	0.6	0.4
532 nm	0.2	0.06	0.1	0.01

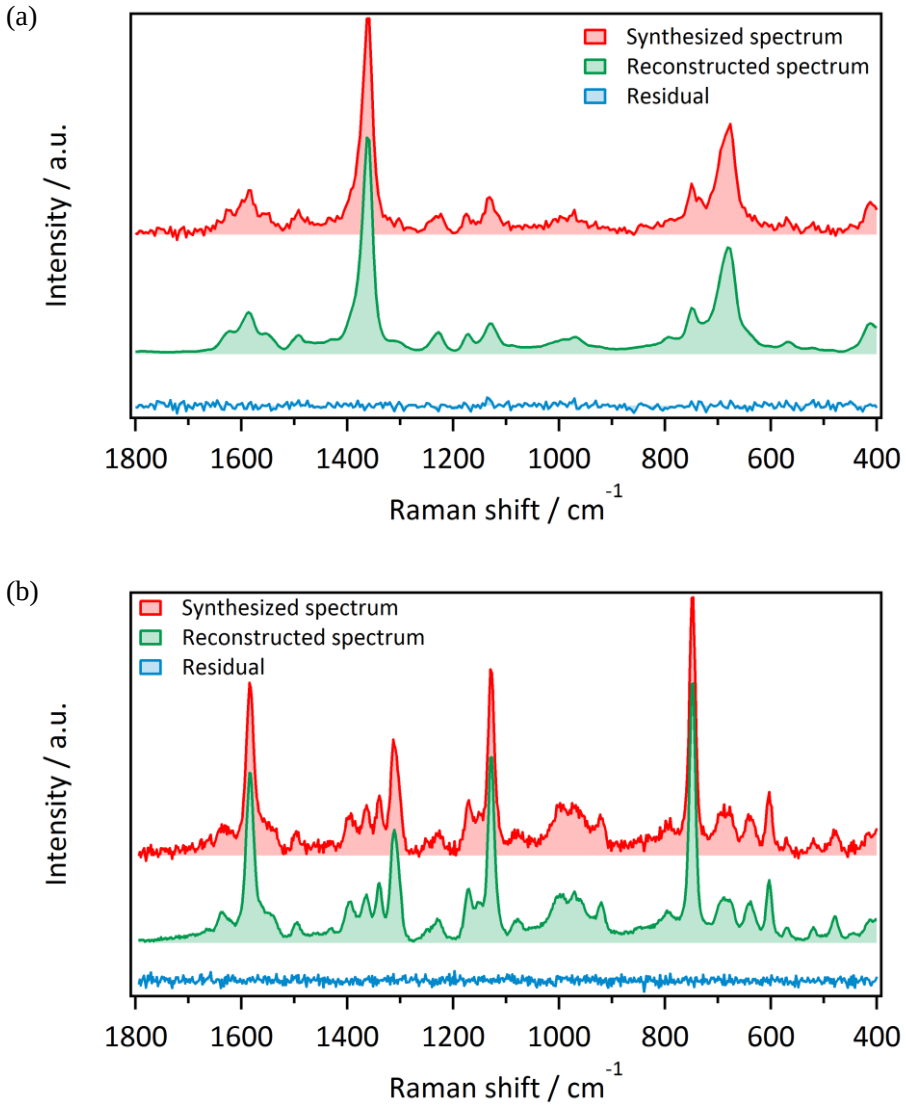

Fig. 2-10 Synthesized Raman spectra and their analysis. (a) 405 nm excitation. (b) 532 nm excitation. In each figure, red spectrum is the synthesized spectrum, green spectrum is the result of fitting, and blue is the differemce between red and green.

2.4. Application to single cell analysis

Based on the result of the comparison between 405 nm and 532 nm, I adopted 405 nm excitation RRS to the analysis of the intracellular redox state of cytochrome species. Following the procedure described in the experimental section, single living HeLa cells were measured. The typically obtained spectrum is shown in Fig. 2-11, red. The spectra obtained from HeLa cells were passed through some data processings, namely background subtraction, intensity correction and fluorescence removal by polynomial fitting technique. The major components in the obtained spectrum was dominated by the Ranan bands of cytochromes, such as the strong bands around 1360 cm^{-1} and 700 cm^{-1} (see Fig. 2-8). This means that the small amount (μM scale) of intracellular cytochrome species can be specifically analyzed by 405 nm excitation RRS.

Since the standard Raman spectra of cytochrome species do not possess any spectral marker bands, the spectral fitting analysis was applied to the spectra obtained from HeLa cells for quantification. In this study, 6 spectra (oxidized cyt b, reduced cyt b, oxidized cyt c, reduced cyt c, bovine serum albumin (BSA) and cover glass) were used as the basis set of the spectral fitting. Since the cells contain not only cytochromes but also huge amount of proteins, addition of the standard spectrum of BSA as a representative of proteins was expected to improve the fitting result. Addition of the spectrum of cover glass was also required to fully subtract the background signals. The green spectrum in Fig. 2-11 corresponds to the result of spectral fitting analysis applied to the red spectrum. The blue spectrum shown in Fig. 2-11 is the difference between the red and the green spectra. There is no spectrally significant residue in the blue spectrum. This fact indicated that the 405 nm excitation RRS and spectral fitting analysis with 6 basis spectra could reconstruct the experimentally obtained spectra. As described in the introduction, the intensity of RRS signal is proportional to the number of molecules. Therefore quantification of the intracellular redox state of cytochrome species could be performed based on the calculated fitting coefficients.

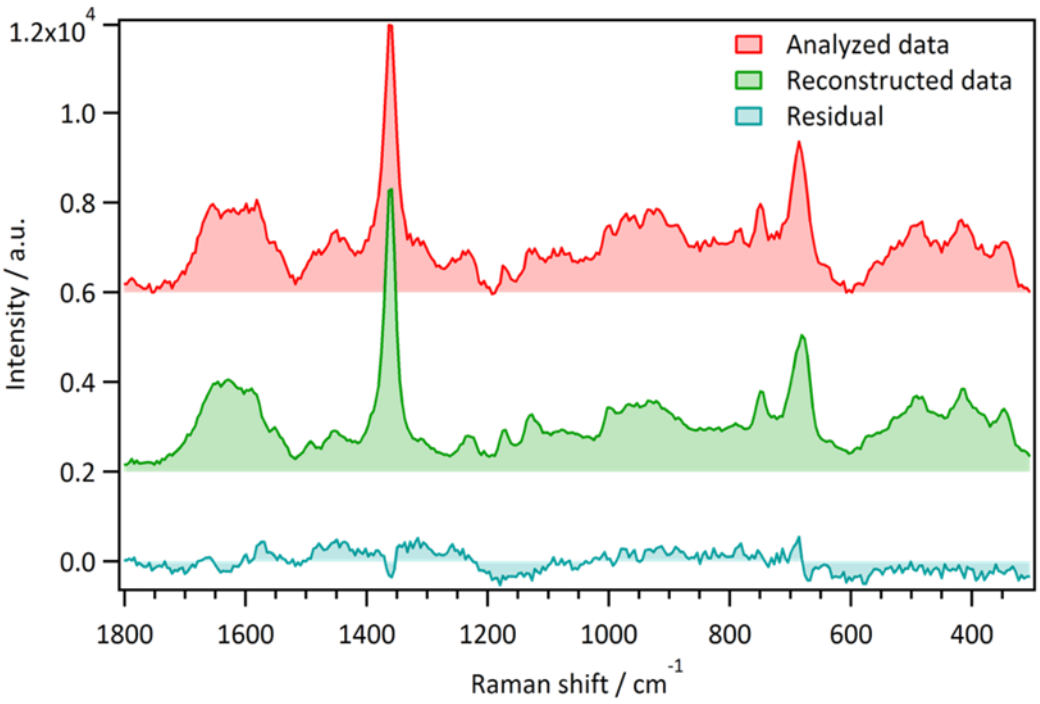

Fig. 2-11 Result of spectral fitting to 405 nm excitation Raman spectra obtained from HeLa cells. Red; experimentally obtained spectrum from a single HeLa cell. Green; reconstructed spectrum of the red by spectral fitting analysis. Blue; difference between the red and the green spectra.

In order to confirm the reproducibility of the current method, I observed more than hundred HeLa cells and checked the distribution of the redox state of cyt b and cyt c. Fig. 2-12 is the histograms of the molar fraction of reduced forms of each cyt b and cyt c. Since the total amount of intracellular cytochromes is dependent on individual cells, the molar fraction is used for discussing the redox alteration in the following. As it was clear, cyt c tended to be kept in reduced state under the current experimental condition, and cyt b showed the middle of reduced and oxidized state. The obtained distribution indicated that the developed 405 nm excitation and spectral fitting analysis could provide reproducible results. If the Gaussian distribution was assumed, the full width of half maximum (FWHM) of the two distributions was calculated as 0.1 for cyt b and 0.04 for cyt c, respectively. These widths of the distribution can be regarded as the sum of dispersion of cellular individuality and experimental error. Thus the calculated FWHM values were considered as the maximum experimental error of the molar fraction of the reduced form determined by the present method.

Next the ability of the developed method to trace the dynamic change of the redox state of cytochrome species inside cells was considered. Dithiothreithol (DTT) is a strong reductant and known to reduce the intracellular molecules[58–60]. I observed the redox state of HeLa cells before and after the addition of DTT into the culture dish. The obtained molar fraction of the reduced forms of cyt b and cyt c is shown in Fig. 2-13. The addition of DTT changed the redox state of cyt b into the more reduced form and the difference was significantly larger than the experimental error elicited above. This shift was consistent with the function of DTT inside the cells. Therefore it was suggested that the developed method could trace the dynamics of the redox state of intracellular cytochrome species.

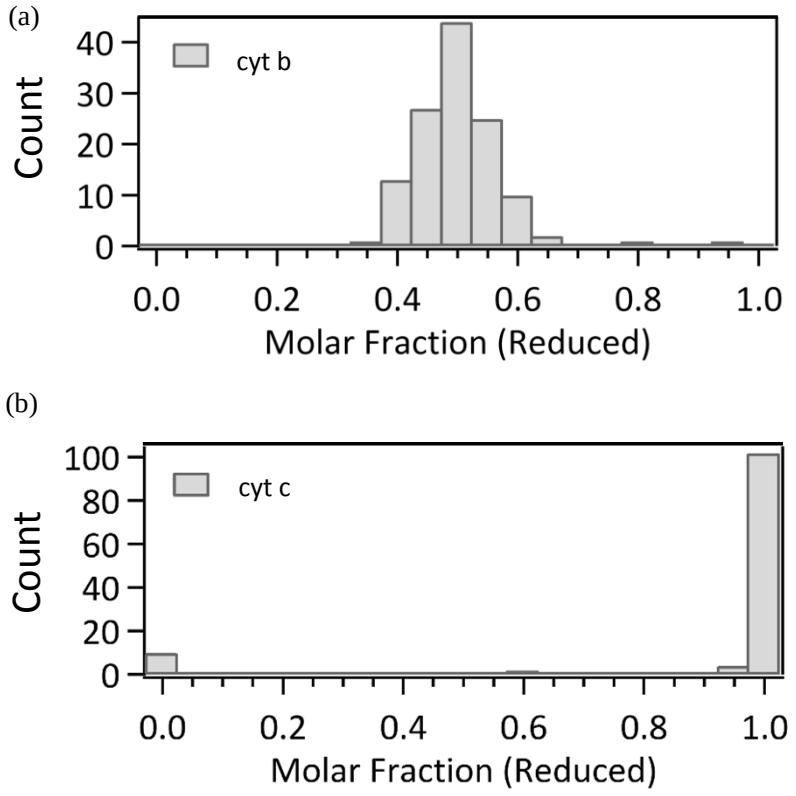

Fig. 2-12 Histograms of the molar fraction of the reduced forms of (a) cyt b and (b) cyt c.

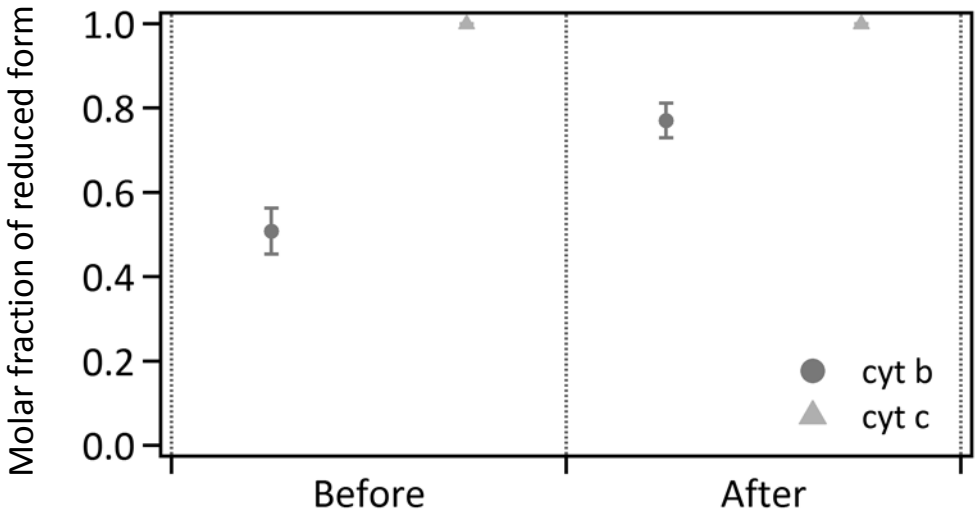

Fig. 2-13 Result of the observing the dynamic change of the redox state of cytochromes induced by DTT addition. Left two plots correspond to the before DTT addition, and right two are after DTT addition.

2.5. Application to the analysis of apoptosis

As described in the chapter 1, cyt c is the initiation signal transduction protein in the apoptotic processes. The abstract of the signal transduction mechanism is described in Fig. 2-14. The release of cyt c from intracellular mitochondria induces the activation of the executor protein of apoptosis, caspase. However, the redox state of the released cyt c, and the relation between the redox state modulation of mitochondrial cytochrome including cyt b and cyt c, and apoptotic signal transduction is not clear yet.

In order to investigate the relation between the redox state and apoptosis, I measured apoptotic HeLa cells. UV-C light was used for stimulation of apoptosis, and the cell viability and redox state were monitored over time. Obtained results are shown in Fig. 2-15. The cell viability (gray bold line in Fig. 2-15a) showed gradual decrease as the time passed. This result indicated that the UV stimulation induced apoptotic process. By comparting the results of the control (culture medium was exchanged to the imaging buffer but no UV irradiation, Fig. 2-15b) and the sample experiment, it was recognizable that cyt c altered its redox state at the middle of the experimental time course though cyt b did not show any significant changes. In the later part of the experiment, the molar fraction of the reduced cyt c showed recovery. This behavior is considered to be originated from the cells of which apoptotic signal transduction was not stimulated. In this experiment, I chose the object at random. In the last part of the experiment, however, most of the cells were dead and only the cells whose apoptotic signal transduction was not triggered, were measurable. Thus I just measured the non-apoptotic cells and apparent recovery of the molar fraction was observed.

The possible reasons of the oxidation during apoptosis are (i) nonspecific oxidation by the production of the strong oxidant such as ROS, and (ii) target specific oxidation such as the enzymatic reaction. According to the previous study, reduced cyt b and cyt c are more stable than oxidized forms, from the thermodynamic point of view[61,62]. In addition, reduced cyt b is inferred to be more labile to oxidation in comparison to reduced cyt c[61, 62]. This fact was

controversial to the observed time course in the apoptosis experiment, namely cyt c was preferentially oxidized and cyt b was not. This result suggested that the nonspecific oxidation was not the reason of the oxidation of cyt c, and the target (cyt c) specific oxidation such as the reaction with cytochrome c oxidase took place during apoptotic signal transduction. At the present, it is difficult to distinguish whether oxidation of cyt c is indispensable for apoptosis or not. However, at least I can conclude that the oxidation of cyt c is a part of the apoptotic signal transduction process.

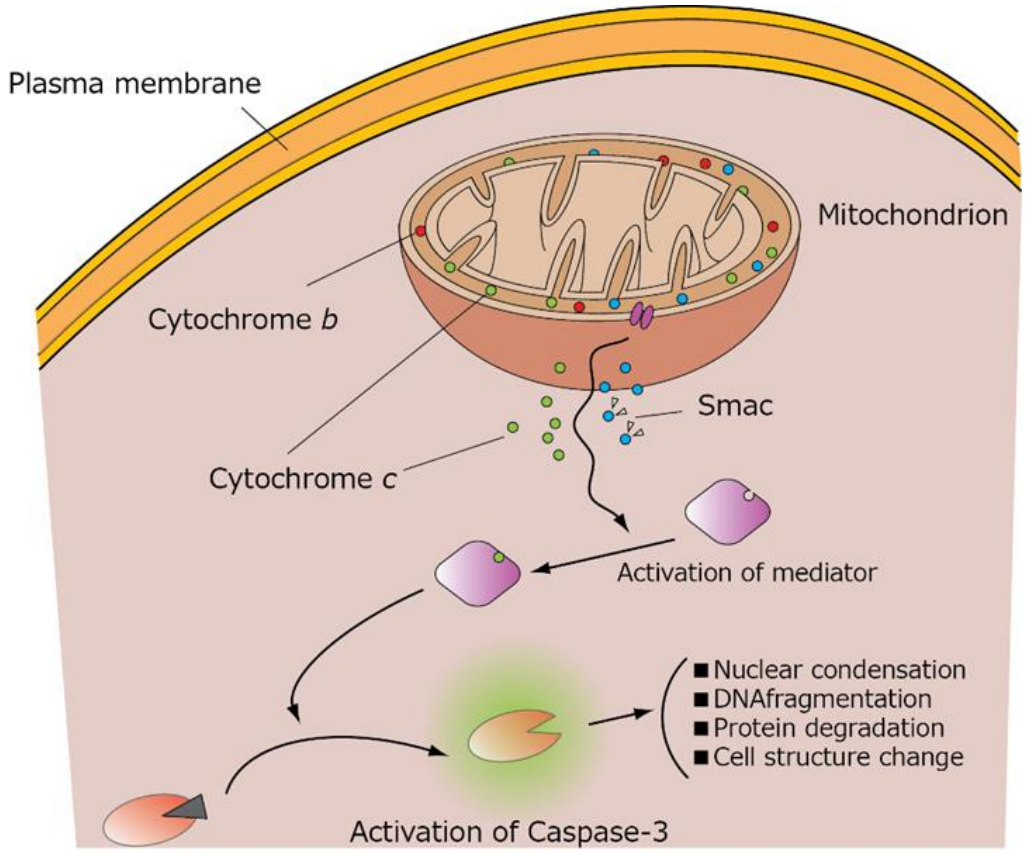

Fig. 2-14 Schematic of the apoptotic signal transduction process in mammalian cells.

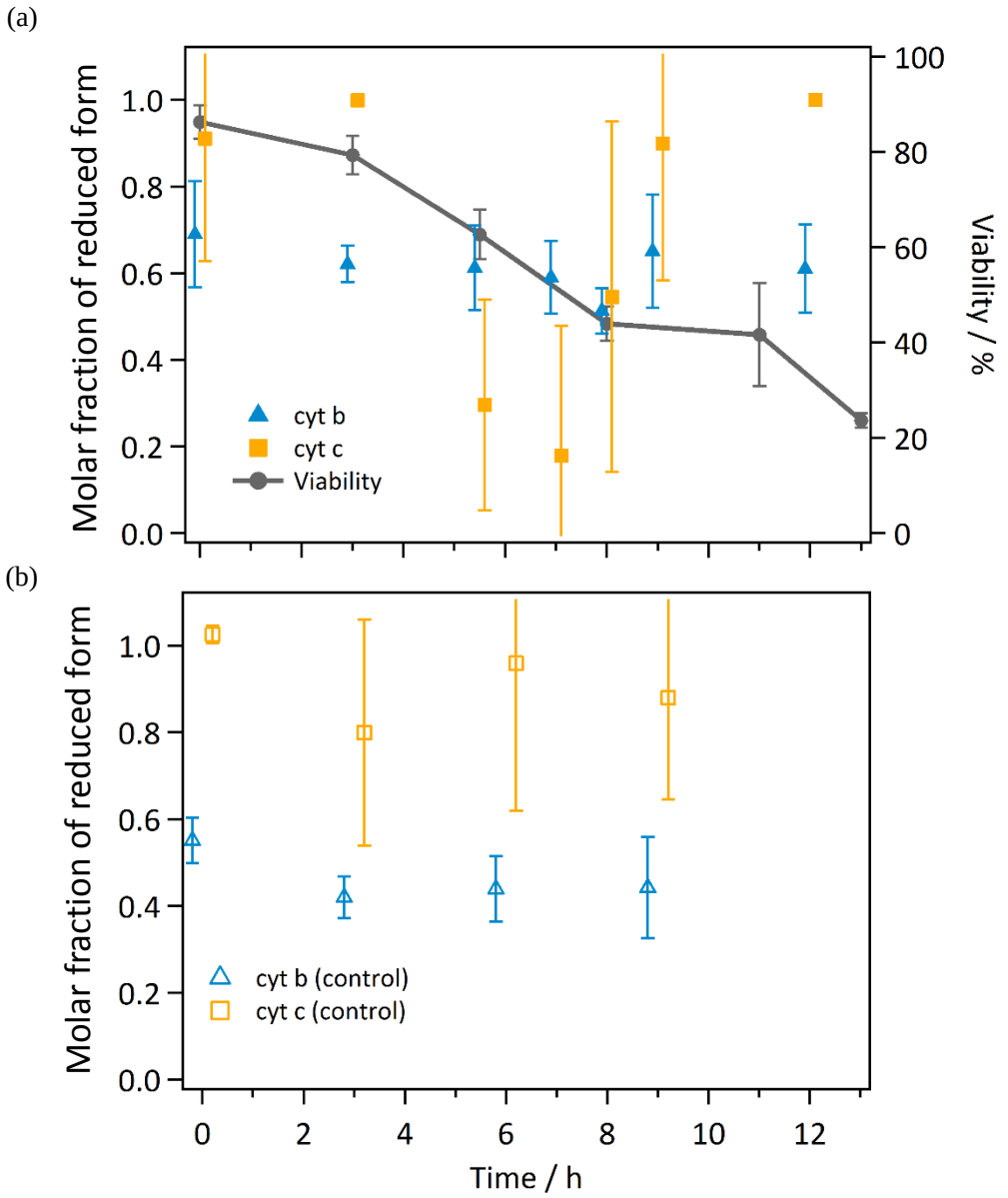

Fig. 2-15 Result of measurement of the apoptotic cells over time. (a) Cell viability curve and time course of redox state of cytochromes after UV irradiation. (b) Result of control experiment.

2.6. Short summary and future prospect

In this chapter, the development of 405 nm excitation RRS microspectroscopy was described. Hemoproteins including cytochrome species are known to possess the electronic transition (absorption bands) in the visible wavelength region. Previously, the application of 532 nm excitation RRS resonant with Q-band (around 550 nm) to redox state analysis of intracellular cytochromes was reported. In this study, I tried to improve the experimental sensitivity and precision by using 405 nm excitation RRS resonant with Soret band (around 410 nm), which stronger enhancement could be expected than Q-band resonant RRS.

Standard spectra measurement of cyt b and cyt c showed that 405 nm excitation scheme was expected to be more useful than 532 nm excitation for quantifying the intracellular redox state of cytochromes due to its strong enhancement of Raman signals. It should be mentioned that 532 nm excitation RRS is also useful if the experimentally obtainable spectra possess the sufficiently strong intensity of signals. Then the applicability of spectral fitting technique for quantifying the intracellular redox state of cyt b and cyt c was confirmed. The experimental error and the ability to trace the dynamic behavior of the intracellular redox state by 405 nm RRS and spectral fitting were evaluated.

At last, redox state alteration during UV-stimulation triggered apoptosis of HeLa cells was observed. 405 nm RRS elucidated that the redox state of cyt c was selectively altered into oxidized state during apoptosis, though that of cyt b was not changed. Taking into consideration the thermodynamic stability, the target selective oxidation of cyt c is considered to be a part of the apoptotic signal transduction process. This is the unique result accessible through the developed 405 nm RRS because previously reported methods are incapable of observing the dynamic behavior of the redox state of cytochromes inside living cells with single cell level resolution.

Presently, the developed method makes us accessible to the ratio of the intracellular cytochrome’s redox state and its dynamic behavior. The spatial information is considered to be

obtainable by changing the spatial averaging method into the mapping method. Further experiment will make it possible to quantify the absolute amount of reduce and oxidized forms of each cytochrome species. The developed method is considered to be applicable to real-time tracing of the redox state during respiration metabolism and signal transduction. This will provide new information useful not only for understanding the basic biology but also for investigating the effect of medicines or the mechanism of disorders related to cytochromes.

Chapter 3

Electronically resonant third-order sum frequency generation microspectroscopy

3.1. Introduction

In the chapter 2, I introduced the development of the nondestructive analytical method which quantifies the intracellular redox state of cytochrome species. In that case, RRS, a kind of linear vibrational spectroscopy, was adopted. In comparison to the linear optical process, the nonlinear optical processes possess some advantages such as high-speed measurement, deep penetration depth and multimodality. In this chapter, I introduce a novel nonlinear spectroscopic technique, electronically resonant third-order sum frequency generation spectroscopy[63].

Third-order sum frequency generation (TSFG) is an analogue of third harmonic generation (THG)[64]. The difference between these two is the number of wavelengths used for signal generation. The schematic diagrams of TSFG and THG are shown in Fig. 3-1. In the case of THG, degenerated photons are used for signal generation. On the other hand, TSFG is generated by two or three differently colored excitation photons (thus TSFG can be regarded as non-degenerated THG). If white-light or supercontinuum are used for excitation light and multi-channel detection is adopted, multiplex TSFG spectrum can be observed[64].

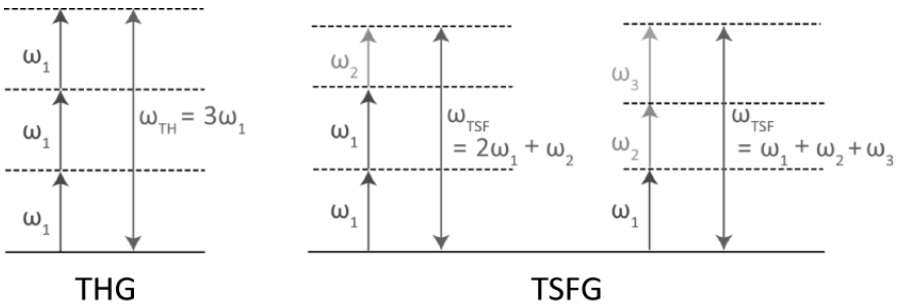

Fig. 3-1 Schematic energy diagrams of THG and TSFG.

Similar to Raman scattering, THG and TSFG are inferred to be resonantly enhanced if one of the virtual states of the nonlinear optical processes and electronic transition of a molecule are close in energy. In fact, electronically resonant THG has been reported[65–70]. In order to confirm and analyze the resonant enhancement of THG, however, scanning of the excitation wavelength is required. Multiplex TSFG can overcome this problem and provide the spectral information on the electronic state of the target molecule. Thus, if the resonant TSFG is available, the information on the redox state of the molecule is possibly elicited from the spectral analysis of resonant TSFG spectra.

Among many hemoproteins, Hb is known as one of the redox active proteins and changes its electronic state in response to the change of its redox state. As is the same with cytochromes, Hb possesses two major absorption bands (Soret band and Q-band). It is thus expected that resonance enhancement of TSFG can be observed if the energy of three virtual states of TSFG process is close to that of either Soret band or Q-band transition. In that case, resonant TSFG is inferred to provide the information on the redox state of Hb. In this chapter, I describe the experimental setup, observed spectra, spectral analysis and signal generation mechanism of resonant TSFG to analyze the redox state of Hb.

3.2. Experimental

3.2.1. Optical system

The schematic of the developed TSFG microscope is depicted in Fig. 3-2. The light source was a cw Q-switched microchip Nd:YAG laser. The fundamental 1064 nm radiation was firstly divided into two. One was used for excitation (ω_1) and the other was introduced into a photonic crystal fiber to generate supercontinuum radiation. This supercontinuum radiation was used as the broad band excitation source (ω_2). Under this condition, the possible combination for the TSFG process is $2\omega_1 + \omega_2$ and $\omega_1 + \omega_2 + \omega_2$'. The 1064 nm and supercontinuum radiations were superimposed after eliminating the spectral components shorter than 1064 nm, and introduced into a modified inverted microscope (ECLIPSE Ti, Nikon). Then the incident light was irradiated onto a sample placed upon a piezo electric stage (Nano-LP200, Mad City Lab) through an objective lens (x40, 0.9 NA, Nikon). Forward propagating signals were collected by the second objective lens (x40, 0.6 NA, Nikon) and the excitation light was removed by a short-pass filter. The signal was introduced into a spectrograph (SpectraPro300i, Princeton Instrument) and detected by a CCD camera (PIXIS 100BR eXcelon, Princeton Instrument).

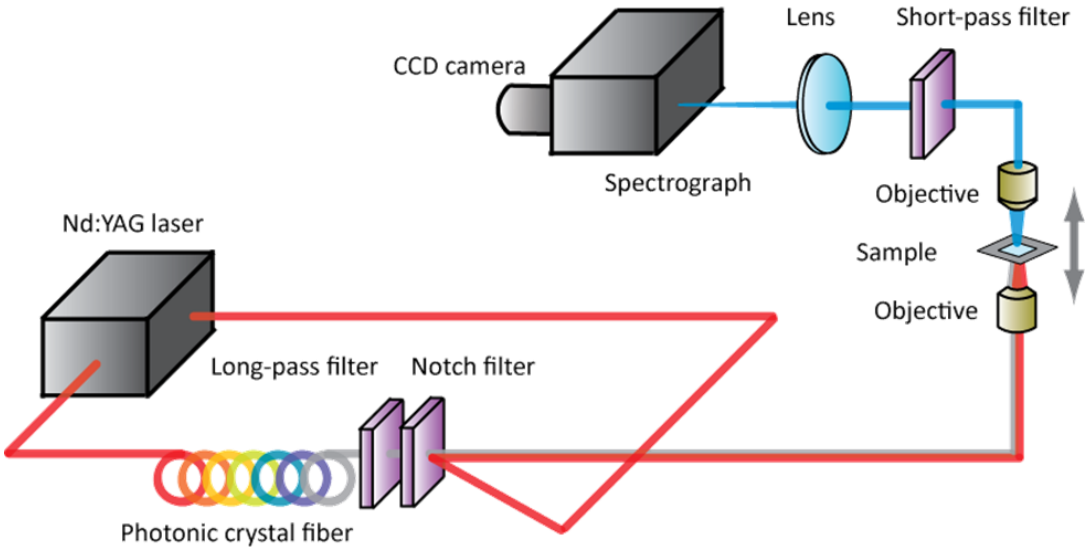

Fig. 3-2 Schematic diagram of the developed TSFG microscope.

3.2.2. Sample preparation and measurement

Cytochrome c solution

In order to confirm the electronic resonance enhancement of TSFG, I firstly tried to measure the signals from dense cyt c solution. Cyt c from bovine heart (Sigma Aldrich Japan) was dissolved in PBS. In resonant TSFG study, I did not control the redox state of cyt c.

Hemoglobin solutions

The Hb samples were purchased from the manufacture. Hb human lyophilized powder (Sigma Aldrich) and Hb A_0, ferrous stabilized human (Sigma Aldrich Japan) were dissolved in PBS after deaeration of the solvent by nitrogen gas. These two samples corresponded to oxidized and reduced samples, respectively. The redox state of Hb solution was checked by UV-visible absorption spectra (Fig. 3-3). The peak position and the spectral shape were consistent with the spectra in the previous studies[71,72]. For control experiment, I made the BSA solution, which did not possess significant absorption in the Soret band wavelength region (Fig. 3-3).

Sample preparation and measurement

The schematic of the sample preparation is depicted in Fig. 3-4. The sample solution was sandwiched by two cover glasses with polystyrene beads of 20 μm in diameter. These beads functioned as a spacer. The two cover glasses were sealed by Vaseline in order to prevent the evaporation of the solution. To observe TSFG signals, the sample was scanned in the axial direction by the piezo stage.

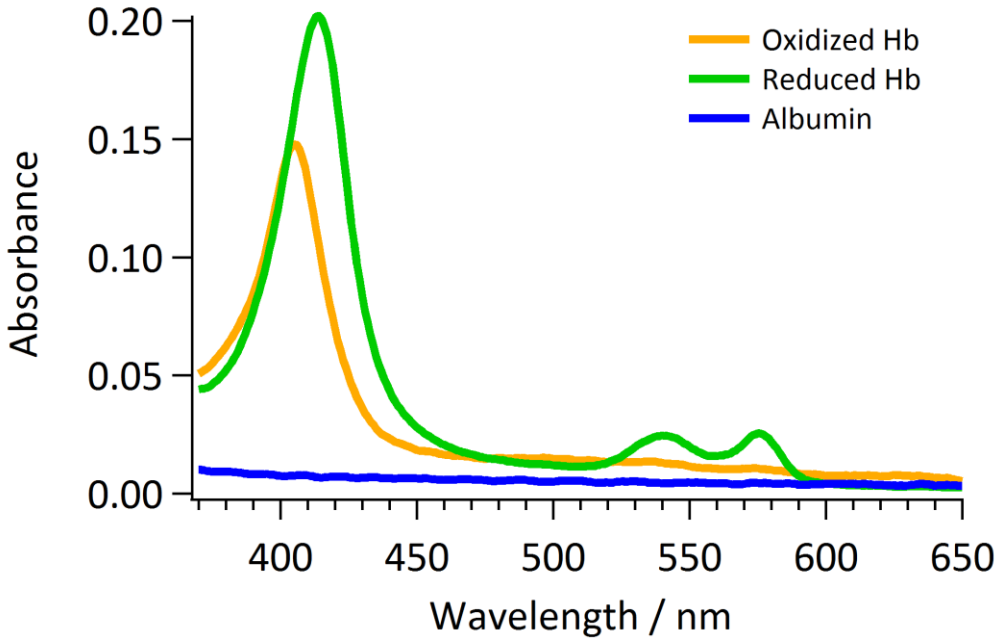

Fig. 3-3 Absorption spectra of reduced and oxidized forms of Hb solutions and BSA solution.

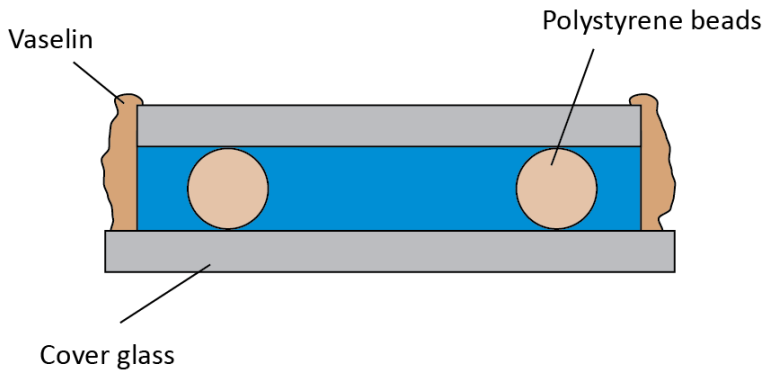

Fig. 3-4 Schematic of the sample preparation for TSFG experiment. The sample solution was sandwiched by two cover glasses with polystyrene beads with 20 μm in diameter. The edge of the cover glass was sealed by Vaselin.

3.3. Resonant TSFG spectra

Figure 3-5 shows the result of TSFG measurement with axial direction scanning of the sample preparation of PBS. From the upper part of Fig. 3-5a, each dark layer corresponds to surrounding atmosphere, upper cover glass, sample solution and lower cover glass, respectively. As it is clear, TSFG signals generated only at the interface between two layers. Though the TSFG signal at the glass-solution interface was quite weaker than that at the glass-atmosphere interface, TSFG from each interface was separately detected (Fig. 3-5b, c).

In the following, the TSFG spectrum obtained from layer A/layer B interface is defined as $I_{a/b}$. Before spectral analysis, I obtained TSFG spectrum of $I_{glass/solution}$ and $I_{glass/atmosphere}$. In order to take account of the aberration under the current experimental condition, TSFG spectra were averaged over ± 2 μm within the peak position in the TSFG intensity plot (Fig. 3-5b, c).

Figure 3-6a is the obtained raw TSFG spectra of the PBS and cyt c solutions ($I_{glass/solution}$). It is noticeable that the wavelength region of TSFG signal is coincide with Soret band absorption (see Fig. 3-3 and Fig. 3-6a). Thus the resonance enhancement of the TSFG signal is expected. In Fig. 3-6a, it is difficult to discuss any significant difference between two raw spectra and thus the TSFG spectra have to be passed through data processing. After background subtraction, $I_{glass/solution}$ was divided by the $I_{glass/atmosphere}$ obtained at the upper glass/atmosphere interface. This manipulation corresponded to the intensity correction of the supercontinuum. It should be noted that the spectrum obtained at the lower glass/atmosphere interface is inappropriate because re-absorption by the sample itself possibly occurs. Resulted TSFG spectra are depicted in Fig. 3-6b. For reference, absorption spectra of cyt c solution is also shown in the same figure. At this stage, the difference between two spectra were recognizable, namely the intensity of TSFG from cyt c solution was stronger than that from the PBS. This result indicates that electronic resonant enhancement of TSFG can take place and is observable by the present experimental setup.

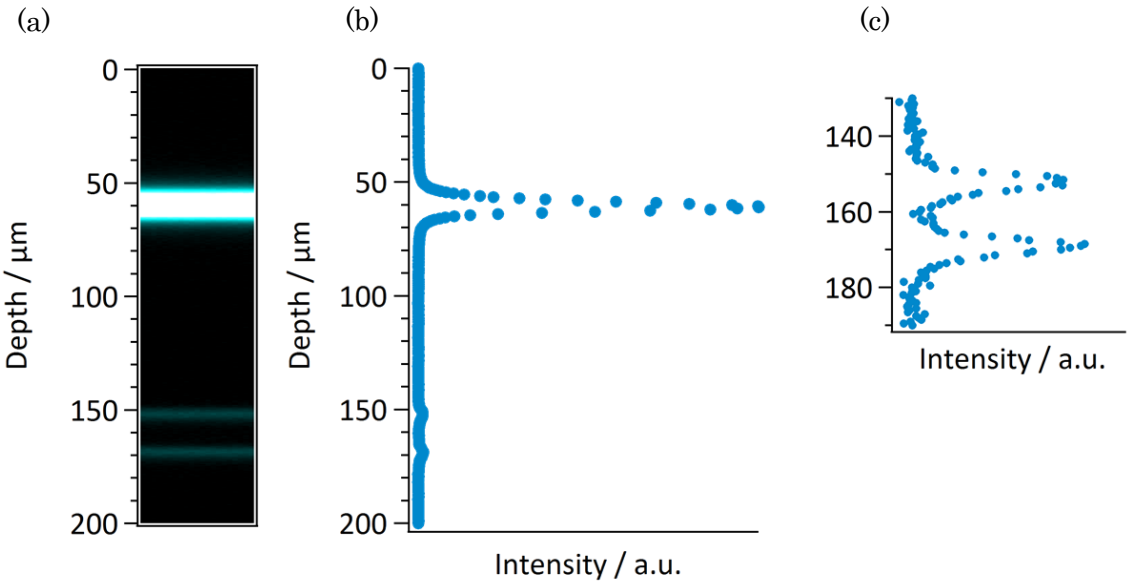

Fig. 3-5 Result of the TSFG measurement of PBS. (a) Obtained image by the axial direction scanning of the sample. (b) Intensity plot of the axial scanning. (c) Expanded plot around the sample solution layer.

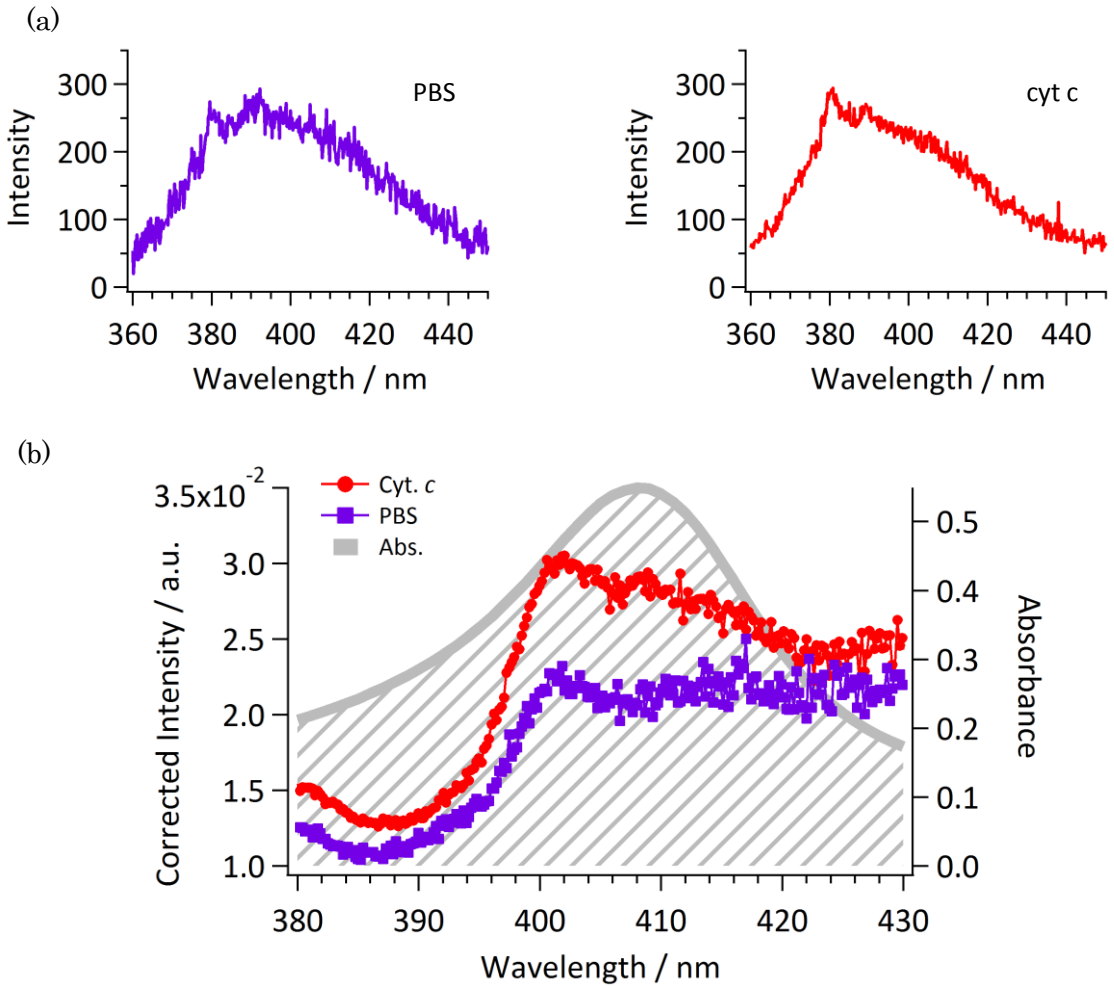

Fig. 3-6 Obtained TSFG spectra and their analysis. (a) Raw TSFG spectra from PBS and cyt c solution. (b) TSFG spectra after intensity correction of the supercontinuum.

3.4. Detailed analysis of resonant TSFG

3.4.1. Resonant TSFG spectra from Hemoglobin solution

I also measured the reduced and oxidized Hb solutions following the same experimental process as the last section. The obtained result was shown in Fig. 3-7a. For reference, absorption spectra of reduced and oxidized Hb solutions are also shown. In this experiment, the BSA solution was measured as negative control. Although the difference between Hb solutions and control (PBS and BSA solution) originated from the resonance enhancement were clear, the difference between reduced and oxidized forms was slight. In addition, despite the fact that there is no electronic resonance in the case of PBS and BSA, the spectral profile of these two control samples was not spectrally flat.

This is possibly because of the aberration under the current tight focusing condition using microscope objective, which cannot be perfectly corrected by $I_{glass/atmosphere}$. In order to normalize the spectral profile, and extract information on electronic resonance effect, the TSFG spectrum of Hb solution was divided by that of PBS. This manipulation was considered as the modification of experimental errors including aberration. In the following, TSFG spectrum divided by that of PBS is defined as normalized TSFG spectrum. Obtained normalized TSFG spectra are shown in Fig. 3-7b. It is noticeable that both absorption and normalized TSFG spectra of reduced Hb show longer peak position in comparison to oxidized Hb. Therefore I can conclude that normalized TSFG spectra qualitatively provide the information on the redox state of Hb.

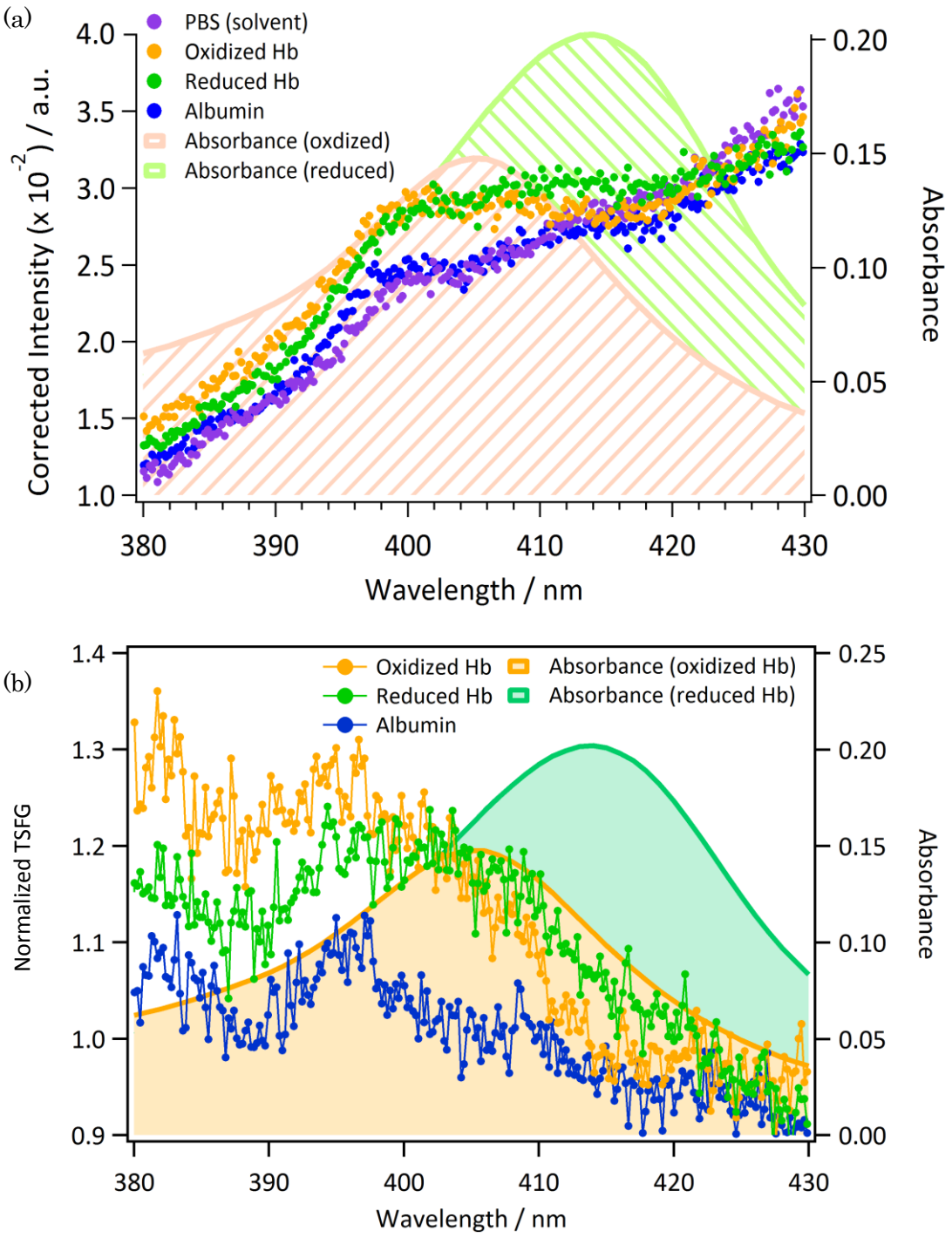

Fig. 3-7 Analyzed TSFG spectra from Hb solutions. (a) TSFG spectra after supercontinuum intensity correction. (b) Normalized TSFG spectra. Absorption spectra of Hbs are also shown for reference.

3.4.2. Signal generation mechanism of TSFG

Although qualitative information on the redox state of Hb could be obtained from TSFG spectra (Fig. 3-7), the spectral shape of the normalized TSFG spectrum was still severely distorted and apparently was not consistent with the absorption spectrum. In order to elucidate the reason of spectral distortion, I theoretically analyzed the signal generation mechanism of TSFG.

In general, the spectral intensity of the coherent nonlinear optical processes can be described by using nonlinear susceptibility,

$$\chi^{(3)} = \chi^{(3)}_{res} + \chi^{(3)}_{nonres}, \tag{1}$$

where $\chi^{(3)}_{res}$ is nonlinear susceptibility of the resonant term and $\chi^{(3)}_{nonres}$ is that of the nonresonant term. Each term in Eq. 1 is described as,

$$\chi^{(3)}_{res} = \frac{A_{res}}{\omega_{res} - \omega_{TSFG} - i\Gamma_{res}}, \tag{2}$$

$$\chi^{(3)}_{nonres} = Ce^{i\theta}, \tag{3}$$

where A_{res} is the amplitude of the resonant term, ω_{TSFG} is the angular frequency of the TSFG signal, ω_{res} is the resonance angular frequency, Γ_{res} is the damping factor of the electronic state, C is the amplitude of the nonresonant term and θ is the relative phase between the resonant and the nonresonant terms. For simplicity, single electronic state is assumed to contribute to resonant signal. Under this assumption, the spectral intensity of the TSFG can be described as,

$$I(\omega_{TSFG}) = \left| \frac{A_{res}}{\omega_{res} - \omega_{TSFG} - i\Gamma_{res}} + Ce^{i\theta} \right|^2. \tag{4}$$

Among many parameters described above, θ is a critical factor which determines the spectral shape of the nonlinear optical process. Thus I theoretically investigated the value of θ.

For the sake of simplicity, the signal generation of THG is treated instead of TSFG and the confocal system which is applicable to the current experimental condition is assumed.

In addition, the optical system is supposed not to possess any aberration. The detailed property of the image formation of the confocal system is described in the previous study[73]. In the following, the coherent transfer function (CTF) is used to discuss the signal generation mechanism of THG. CTF is the Fourier transform of the amplitude spread function (ASF) of the optical system which consists of the excitation and collection systems. In third order nonlinear coherent microscopy, the ASF corresponds to the product of the cube of the excitation field formed by the excitation system and the signal field formed by the collection system. The ASF corresponds to the image amplitude distribution of a single point object obtained by the total system. It is notable that ASF possesses the information on the phase of the light, which cannot be discussed by frequently used point spread function. By using ASF, the image amplitude formed by the object with the nonlinear susceptibility $\chi^{(3)}(x, y, z)$ through the nonlinear optical microscopy is described as,

$$A(x', y', z') = \int_{-\infty}^{\infty}\int_{-\infty}^{\infty}\int_{-\infty}^{\infty} \chi^{(3)}(x-x', y-y', z-z')\mathrm{ASF}(x, y, z)dxdydz, \quad (5)$$

where the coordinate (x', y', z') indicates the displacement of the sample stage from the origin, $\chi^{(3)}(x, y, z)$ corresponds to the distribution of nonlinear optical susceptibility of the object, and ASF (x, y, z) is the ASF[74]. The image intensity is calculated as the square of the modulus of the image amplitude $A(x', y', z')$.

First, the semi-infinite slab defined by the following nonlinear optical susceptibility is considered,

$$\chi_{\mathrm{step}}^{(3)}(x, y, z) = \chi_0^{(3)}u(z) = \begin{cases} 0 & (z < 0) \\ \chi_0^{(3)} & (z \geq 0) \end{cases}, \quad (6)$$

where $u(z)$ represents the step function. The value of $\chi_0^{(3)}$ is dependent on the nonlinear optical process. In the current experimental condition, the sample stage is scanned in the z direction

(direction of the optical axis), and the excitation and collection systems are unchanged. In other words, the center of the ASF is unchanged and fixed at the origin. The image amplitude of the semi-infinite slab (the complex amplitude of the signal for each depth position of the interface), $A_{\text{step}}(z')$, is expressed as follows,

$$\begin{aligned} A_{\text{step}}(z') &= \int_{-\infty}^{\infty}\int_{-\infty}^{\infty}\int_{-\infty}^{\infty} \chi^{(3)}_{\text{step}}(x-x', y-y', z-z')\text{ASF}(x, y, z)dxdydz \\ &= \chi^{(3)}_{0} F(z'), \end{aligned} \tag{7}$$

with

$$F(z') = \int_{z'}^{\infty}\int_{-\infty}^{\infty}\int_{-\infty}^{\infty} \text{ASF}(x, y, z)dxdydz = \sum_{z=z'}^{\infty} \alpha(z)\Delta z, \tag{8}$$

and

$$\alpha(z)\Delta z = \int_{z}^{z+\Delta z}\int_{-\infty}^{\infty}\int_{-\infty}^{\infty} \text{ASF}(x, y, z)dxdydz, \tag{9}$$

where the displacement of the sample stage z' corresponds to the depth position of the interface relative to the ASF center (origin). $F(z')$ is determined by the ASF and is independent of the nonlinear optical susceptibility. Eq. 7, 8 mean that the total intensity of the signal is described as the summation of the contribution from each small segment of the ASF. Using Fourier transformation, $F(z')$ is expressed as the inverse Fourier transform of the product of the CTF and $U(f_x, f_y, f_z)$, where

$$U(f_x, f_y, f_z) = \frac{1}{2}\delta(f_x)\delta(f_y)\left\{\delta(f_z) + \frac{i}{\pi f_z}\right\}, \tag{10}$$

which is the Fourier transform of the step function $u(z)$. Here $\delta(f)$ is the Dirac's delta function. Therefore, $F(z')$ is described as

$$
\begin{aligned}
F(z') &= \frac{1}{2}\int_{-\infty}^{\infty}\int_{-\infty}^{\infty}\int_{-\infty}^{\infty} \mathrm{CTF}(f_x, f_y, f_z)\delta(f_x)\delta(f_y)\left\{\delta(f_z)+\frac{i}{\pi f_z}\right\} \\
&\quad \times \exp\left[i2\pi(f_x x' + f_y y' + f_z z')\right] df_x df_y df_z \\
&= \frac{1}{2}\int_{-\infty}^{\infty} \mathrm{CTF}(0, 0, f_z)\left\{\delta(f_z)+\frac{i}{\pi f_z}\right\}\exp\left[i2\pi f_z z'\right] df .
\end{aligned}
\tag{11}
$$

For later use, the function $F'(z')$ is defined as

$$
F'(z') = \int_{-\infty}^{z'}\int_{-\infty}^{\infty}\int_{-\infty}^{\infty} \mathrm{ASF}(x, y, z)\,dx\,dy\,dz . \tag{12}
$$

$F'(z')$ also can be expressed as the inverse Fourier transform of the product of the CTF and $U'(f_x, f_y, f_z)$, where

$$
U'(f_x, f_y, f_z) = \frac{1}{2}\delta(f_x)\delta(f_y)\left\{\delta(f_z)-\frac{i}{\pi f_z}\right\}, \tag{13}
$$

which is the Fourier transform of $u(z)$. Then $F'(z')$ is described as,

$$
F'(z') = \frac{1}{2}\int_{-\infty}^{\infty} \mathrm{CTF}(0, 0, f_z)\left\{\delta(f_z)-\frac{i}{\pi f_z}\right\}\exp\left[i2\pi f_z z'\right] df_z . \tag{14}
$$

In the following, the value of $F(0)$ is discussed as a critical factor for the coherent buildup of the signal in homogeneous medium. $F(0)$ is proportional to the complex amplitude of the signal when the interface locates at the center of the ASF (Eq. 7), and is given by

$$
F(0) = \frac{1}{2}\int_{-\infty}^{\infty} \mathrm{CTF}(0, 0, f_z)\left\{\delta(f_z)+\frac{i}{\pi f_z}\right\} df_z . \tag{15}
$$

$F(0)$ is subject to $\mathrm{CTF}(0, 0, f_z)$ which depends both on the nonlinear optical process and on the NAs of the excitation and collection systems.

Next, the homogeneous medium is considered. If the excitation beam is focused into

the homogeneous medium with the constant nonlinear optical susceptibility $\chi_0^{(3)}$, the signal amplitude A_{homo} can be described as

$$\begin{aligned} A_{\mathrm{homo}} &= \chi_0^{(3)} \int_{-\infty}^{\infty}\int_{-\infty}^{\infty}\int_{-\infty}^{\infty} \mathrm{ASF}(x, y, z)dxdydz \\ &= \chi_0^{(3)} \{F(z') + F'(z')\} \\ &= \chi_0^{(3)} \{F(0) + F'(0)\} \\ &= \chi_0^{(3)} \{F(0) + F^*(0)\}. \end{aligned} \tag{16}$$

In the above equation, the relation of ASF(x, y, z) = ASF*(x, y, z) is used. Herein the factor $\cos\theta_{\mathrm{F}}$, where $\theta_{\mathrm{F}} = \mathrm{Arg}[F(0)]$, is introduced. This value indicates the degree of coherent buildup and varies from 0 to 1. In particular, if $\cos\theta_{\mathrm{F}} = 1$, the "constructive buildup" occurs. On the other hand, if $\cos\theta_{\mathrm{F}} = 0$, the "destructive buildup" takes place. In the latter case, the signal from each point in the ASF is canceled out and significant signals are unavailable.

The CTF of THG microscopy has an asymmetric profile, namely the value of CTF(0, 0, f_z) becomes nonzero only in the positive f_z domain, and is zero in the negative f_z domain and at the origin[73]. This asymmetric CTF results in the distinguishing coherent buildup of the THG signal. Because the CTF is a positive real function, $F(0)$ for THG microscopy becomes a pure imaginary number with the asymmetry of the CTF mentioned above (Eq. 15). Consequently, the factor $\cos\theta_{\mathrm{F}}$ becomes zero ($\theta_{\mathrm{F}} = \pi/2$), and the signal generation of THG results in the destructive buildup. It is also shown by Eq. 16, in which the signals from the upper part $F(0)$ and the lower part $F^*(0)$ in the ASF are canceled out if $F(0)$ is pure imaginary number. In THG microscopy with a high-NA excitation system, irrespective of the NAs of the excitation and collection systems, the CTF has the asymmetric profile[73]. As a result, the factor $\cos\theta_{\mathrm{F}}$ for THG microscopy inevitably becomes zero. This fact indicates that THG microscopy necessarily causes the destructive buildup regardless of the NAs of the excitation and the collection systems. This destructive buildup corresponds to the well-known phase mismatch under THG microscopy[75,76].

In contrast, if the CTF is nearly symmetric around the origin and CTF(0, 0, 0) is non-

zero, the imaginary part of $F(0)$ is canceled out and the real part remains (see Eq. 15). In this case, $F(0)$ approaches a real number ($\cos\theta_F \approx 1$). As a result, $F(0) + F^*(0)$ becomes a large value, leading to the constructive buildup of the signal (Eq. 16). This means that the strong signal is generated from the homogeneous medium if $\cos\theta_F \approx 1$.

Figure 3-8 illustrates how the signals of THG microscopy builds up in the case where the excitation beam is focused into the homogeneous medium through a higher-NA excitation system than the collection system. In Fig. 3-8, the red arrows indicate the contributions from each segment in the ASF to the total signals (Eq. 9). It should be noted that each contribution possesses both the amplitude and the phase factors. In THG microscopy, the phase of the signal from each segment drastically changes. This rapid modulation of the phase causes the destructive buildup. The sum of all arrows for THG microscopy in Fig. 3-8 reaches the imaginary axis (blue arrows), in other words, $F(0)$ for THG microscopy is a pure imaginary number ($\cos\theta_F = 0$).

The destructive buildup of THG signal is depicted in Fig. 3-9, in which the contributions of the upper parts and lower parts from the ideal plane in the ASF are separately indicated. The depth position of the ideal plane is defined as z'. Note that Fig. 3-9 is independent of the value of the nonlinear optical susceptibility which is a complex number in general depending on the electronically resonant condition. Since the function CTF(0, 0, f_z) for THG microscopy has zero values in the negative f_z domain and at the origin, $F(z')$ (Eq. 11) becomes

$$F_{\mathrm{THG}}(z') = \frac{1}{2}\int_0^\infty \frac{i}{\pi f_z}\mathrm{CTF}(0,0,f_z)\exp\left[i2\pi f_z z'\right]df_z. \tag{17}$$

Likewise, $F'(z')$ for THG microscopy [Eq. (14)] becomes

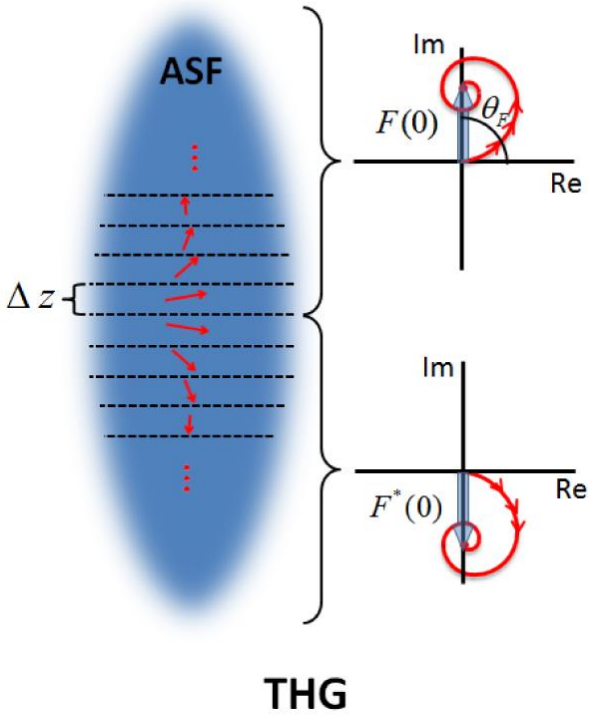

Fig. 3-8 Contribution of each section in ASF of THG microscopy to the THG signal. Red arrows indicate complex numbers in complex plane. The summations of the contribution of each section for the upper and lower parts are shown by the blue arrow in the right part of the figure.

$$F'_{\mathrm{THG}}(z') = -\frac{1}{2}\int_0^{\infty} \frac{i}{\pi f_z}\,\mathrm{CTF}(0,0,f_z)\exp\left[i2\pi f_z z'\right]df_z. \tag{18}$$

Therefore, the relation of $F_{\mathrm{THG}}(z') = -F'_{\mathrm{THG}}(z')$ is obtained. This relationship means that, in the case of the homogeneous medium, the contributions of the upper part $F_{\mathrm{THG}}(z')$ and lower part $F'_{\mathrm{THG}}(z')$ from the ideal plane differ by π in phase regardless of the position of the ideal plane. This constant anti-phase relationship around the ideal plane results in the disappearance of the THG signal (destructive buildup). This implies that θ in Eq. 4 should be π.

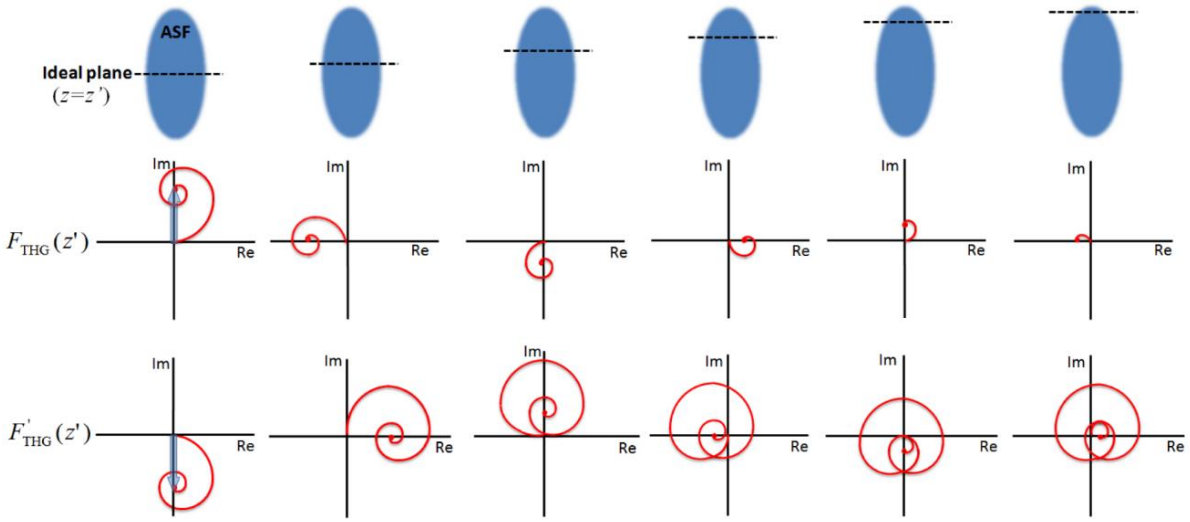

Fig. 3-9 Schematic of destructive buildup of THG signal. The top figures illustrate the ASFs of THG microscopy and the ideal planes. The middle figures describe the buildup of THG signal generated from the part above the ideal plane, representing the sum of the THG complex amplitudes that correspond to the arrows in Fig. 3-8. The bottom figures depict the buildup of THG signal generated from the part below the ideal plane. The leftmost figures show the case where the ideal plane is located in the center of the ASF.

As experimentally shown in Fig. 3-5, THG microscopy generates the signal only at the interface if the sample object can be regarded as the semi-infinite slab. Figure 3-10 illustrates the image amplitude of the semi-infinite slab which is proportional to $F_{THG}(z')$, and the image intensity which is proportional to square of modulus of $F_{THG}(z')$ ($|F_{THG}(z')|^2$). In Fig. 3-10, the curves of $\mathrm{Re}[F_{THG}(z')]$, $\mathrm{Im}[F_{THG}(z')]$ and $|F_{THG}(z')|^2$ are plotted. The figures in the middle row of Fig. 3-9 correspond to the curves on the right side from the dashed line in Fig. 3-10.

In the present study, the resonant TSFG signal was generated only from the sample solution. Although the nonresonant TSFG signal was generated from both the solution and the glass, the nonresonant signal from the glass was inferred to be more intense than that from the solution. In addition, the phases of the nonresonant signals from the glass and the solution differ by π. Consequently, the total nonresonant TSFG signal approximately had the identical phase with the that from the glass due to the partial cancelation between the signals from glass and solution. Thus, the phase difference between the resonant TSFG signal and the nonresonant TSFG signal was inevitably π regardless of the position of the interface between the solution and the glass ($\theta = \pi$).

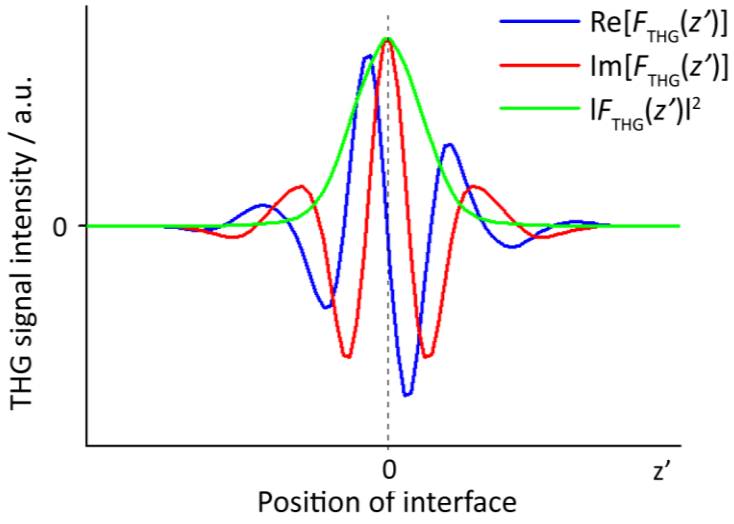

Fig. 3-10 The THG intensity and the THG complex amplitude acquired by scanning the interface in z direction.

3.4.3. Mathematical simulation of the resonant TSFG spectra

Based on the discussion in the last section, numerical simulation of the obtained normalized TSFG spectra of oxidized and reduced forms of Hb was performed. The conclusion of the last section is that the spectral distortion of normalized TSFG spectra was the result of coherent interference between the nonresonnat and resonant terms, and the relative phase difference between the two terms (the value of θ in Eq. 4) was estimated as π under the current experimental condition. The parameters of ω_{res} and Γ_{res} in Eq. 4 were speculated from the absorption spectra, namely the ω_{res} was estimated from the peak position of the absorption spectrum and Γ_{res} was estimated from the width of the absorption spectrum.

Simulated normalized TSFG spectra are shown in Fig. 3-11 by the bold lines. The mathematical simulation reproduced the general forms of the experimentally obtained normalized TSFG spectra. The minor inconsistence between the experimental spectra and the simulated spectra were found around 390 nm. The reason of the inconsistence is not clear yet, but some experimental or analytical processes are considered to be related, because all normalized spectra including those of Hb solutions and BSA solution possess the same spectral shape around 390 nm (Fig. 3-7). This result indicates that the redox state and the electronic state of Hb can be investigated through the spectral analysis of resonant TSFG spectra.

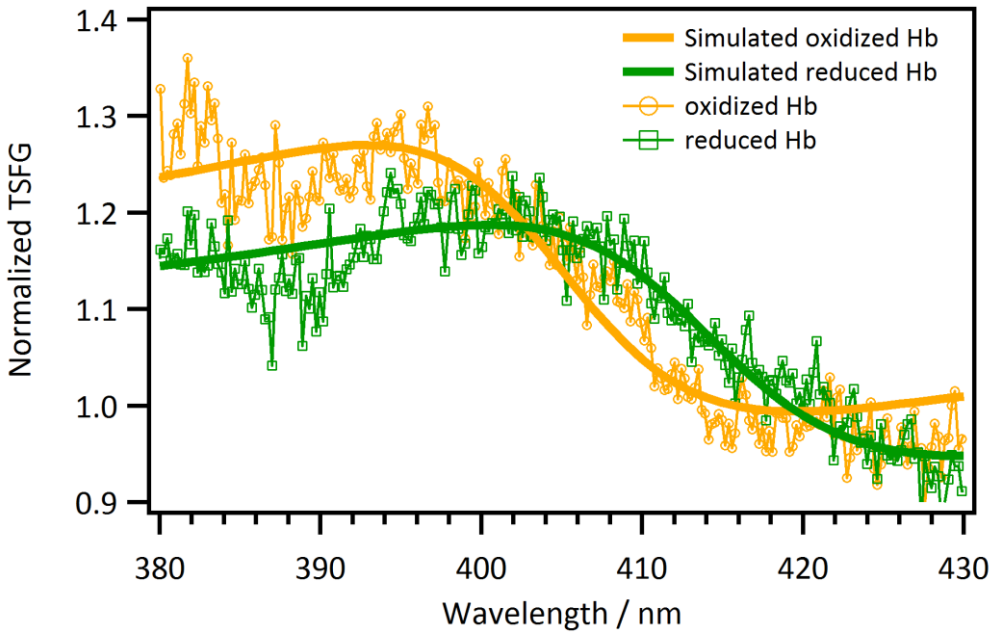

Fig. 3-11 Obtained normalized TSFG spectra and simulated TSFG spectra. Thin lines are obtained spectra, and bold lines are simulated spectra. Green lines are results of the reduced Hb and orange lines are those of the oxidized Hb.

3.5. Short summary and future prospect

In this chapter, the development of electronically resonant TSFG microspectroscopy was introduced. TSFG is a non-degenerated analog of THG. By using white-light excitation, TSFG spectrum is accessible. Since TSFG takes place as a result of the interaction with three virtual states, resonance enhancement is expected to be observed if the energy of one of the virtual states and that of the electronic transition of the molecule is close to each other. Resulted resonant TSFG spectrum possibly provides the information on the molecular electronic state and the redox state.

In order to confirm resonance enhancement, TSFG spectra from hemoprotein solutions were observed. In comparison to the control spectra from the solvent and the BSA which was not resonant under the current experimental condition, TSFG spectra from hemoproteins showed clear enhancement of the signal. Thus electronically resonant TSFG was confirmed.

On the other hand, obtained TSFG spectra showed severely distorted spectral shapes. The reason of the distortion was theoretically analyzed using ASF. It was revealed that the contributions to the total TSFG signal from the former and latter part of ASF possess the same amplitude but are kept in anti-phase relation. Moreover, this result is irreverent to the position of the interface inside ASF. By applying this result to the current experimental condition, it was required that the relative phase between the resonant and nonresonant terms of the TSFG's nonlinear susceptibility should be π.

Based on this result, the resonant TSFG spectra were mathematically simulated. Although the small inconsistency was found presumably due to optical aberration and other experimental errors, the general shape of the resonant TSFG spectra were reproduced by mathematical simulation. Therefore it was concluded that the redox state of Hb could be directly analyzed through the detailed spectral analysis of resonant TSFG.

The redox state of Hb is deeply related to the human disorders, not only limited to the difference of the ability to transport the oxygen molecules. For example, the redox state of Hb plays important role in malaria, in which the person possessing larger contents of oxidized Hb than usual shows resistance against the causal protozoa[77]. Therefore, the detailed redox state analysis of Hb inside the life body possibly provides the important knowledge to treat malaria disease. The analysis of the toxic gases is another example which Hb's redox state and electronic state are deeply related. In forensic science, identification of the Hb's electronic state is useful to analyze toxic gases such as hydrogen sulfate, carbon monoxide and hydrogen cyanide. The application of TSFG to this analysis fastens the analytical time because TSFG is an interface sensitive technique and will not require the complicated pretreatment to measuring the blood sample. Hence, further development and experiment of the resonant TSFG technique will offer plenty of information on Hb and related biological functions.

Chapter 4

Attempt to apply TSFG microspectroscopy to biological sample; cornea study

4.1. Introduction

In the chapter 3, I introduced multiplex TSFG microspectroscopy and resonant TSFG spectroscopy. In that study, the sample was homogeneous solution with Hb and any applications of TSFG spectroscopy to biological samples were not described.

In this chapter, the application of TSFG microspectroscopy to *ex vivo* imaging of the rat corneal tissue is introduced. As mentioned in the chapter 3, TSFG is one of the nonlinear optical processes, which attract enormous attention in the field of bioimaging due to their properties such as high speed measurement, deep penetration depth and intrinsic three-dimensional sectioning capability[64,78–93]. Among these characters, multimodality of the nonlinear optical process makes itself a powerful analytical technique for biological samples. When the intrinsic light is irradiated onto the sample, various nonlinear optical processes can simultaneously take place[94–96]. Since each process takes place based on the different contrast mechanism, simultaneous detection of various nonlinear optical processes provides plenty of structural and molecular information inside the biological sample without any labeling and destructive processes.

In this chapter, first I introduce the optical setup and the obtained signal other than TSFG. The contrast mechanism of each nonlinear optical process is shortly described because it is of great importance to interpret the obtained images. Then the abstract of the sample, rat cornea, is described. At last, the application of the developed optical system to the imaging of rat cornea is introduced and what can be observed by the TSFG and the other nonlinear optical processes is described.

4.2. Experimental

4.2.1 Optical setup

The schematic of the developed nonlinear spectral microscope is depicted in Fig. 4-1. This optical system can be regarded as the extension of the TSFG microscope described in the chapter 3. The light source was a cw Q-switched microchip Nd:YAG laser. The fundamental 1064 nm radiation with 800 ps pulse width was firstly divided into two. One was used as excitation radiations, and the other was introduced into a photonic crystal fiber. Supercontinuum radiation generated from the photonic crystal fiber passed through long-pass filters, and superposed by a notch filter with the 1064 nm radiation. Two radiations were then introduced into a modified inverted microscope (ECLIPSE Ti, Nikon) and irradiated onto a sample through an objective lens (CFI Plan Apo 60×/NA 1.2, Nikon). The sample was placed upon a piezo electric stage to perform raster scanning. The generated signals were collected by a second objective lens (Apo NIR 60×/NA 1.0, Nikon) and divided into two, namely into the visible components and the near-infrared components, by a dichroic mirror. The visible signal passed through short-pass filters, and introduced into a spectrograph (SpectraPro 300i, Princeton Instrument). The signal was detecetd by an air-cooled CCD camera (PIXIS 100BR eXcelon, Princeton Instrument). For the near-infrared component, the signal passed through short-pass filters and a notch flter, and introduced into a spectrograph (LS785, Princeton Instrument). The signal was detected by an air-cooled CCD camera (PIXS 100BR, Princeton Instrument).

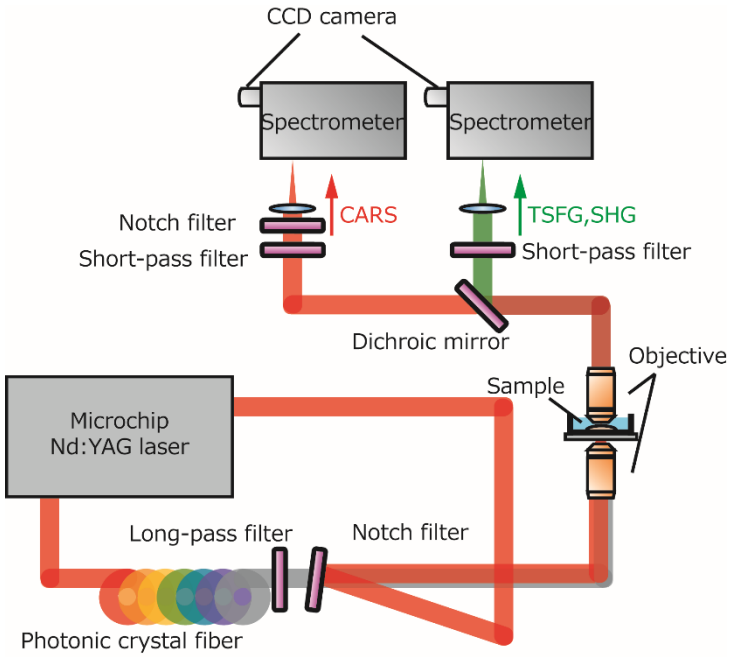

Fig. 4-1 Schematic diagram of the developed nonlinear spectral microscope.

4.2.2. Sample preparation

12- to 16-week-old male Long Evans rats, each weighing 250 g to 400 g (Charles River Laboratories), were used. All animals were treated in accordance with the ARVO Statement for the Use of Animals in Ophthalmic and Vision Research. Experimental protocols were approved from the animal ethics review board in University of Tsukuba. Each rat was anesthetized by intraperitoneal injection of pentobarbital (25 mg/kg of body weight). Under an operating microscope, corneas of the eyes were excised. The corneas were immediately soaked in normal saline, and then placed between a glass bottom dish and a cover glass.

4.3. Observed nonlinear optical processes

Typical obtained spectra from the cornea sample are depicted in Fig. 4-2. All spectra shown in the Fig. 4-2 were generated from different positions of the cornea. In the visible wavelength region, TSFG was detected around 400 nm as a broad band signal. The sharp peak at 532 nm corresponded to the signal of second harmonic generation (SHG). Next to SHG, second-order sum frequency generation (SFG) signal was also detected. In the near-infrared region, sharp bands on the broad background were detected. These signals corresponded to those of coherent anti-Stokes Raman scattering (CARS).

Correct understanding of the contrast mechanism of each nonlinear optical process is of great importance in order to interpret the obtained image by each process. SHG (and SFG) signal is obtainable from the non-centrosymmetric structure because the nonlinear susceptibility of SHG is zero if the system is symmetric. Therefore, SHG is sensitive to the filamentous structure such as collagen fibers[97,98], myosin filament[99,100] and microtubules[101,102]. On the other hand, CARS is one of the third-order Raman processes and its contrast mechanism is the same as that of spontaneous Raman scattering. The CARS spectra thus contain the information on molecular vibration and structure[88,90,94,103]. However, obtained multiplex CARS spectra showed dispersive line shapes (Fig. 4-2). This distortion is originated from the interference between the resonant and the nonresonant signals, which is directly elucidated from Eq. 4 in the chapter 3. Moreover, due to the coherent interference of the process, the intensity of the obtained CARS spectra was not linear to the number of molecules. This made the interpretation of the obtained spectra quite difficult.

In order to retrieve linear and non-distorted spectra from raw multiplex CARS spectra, the maximum entropy method (MEM) and time-domain Kramers-Kronig transformation have been developed[104–107]. In this study, MEM was applied in order to obtain Im[$\chi^{(3)}$] spectra, where $\chi^{(3)}$ means the third-order nonlinear susceptibility. Im[$\chi^{(3)}$] spectra provide the same information as that spontaneous Raman spectra supply.

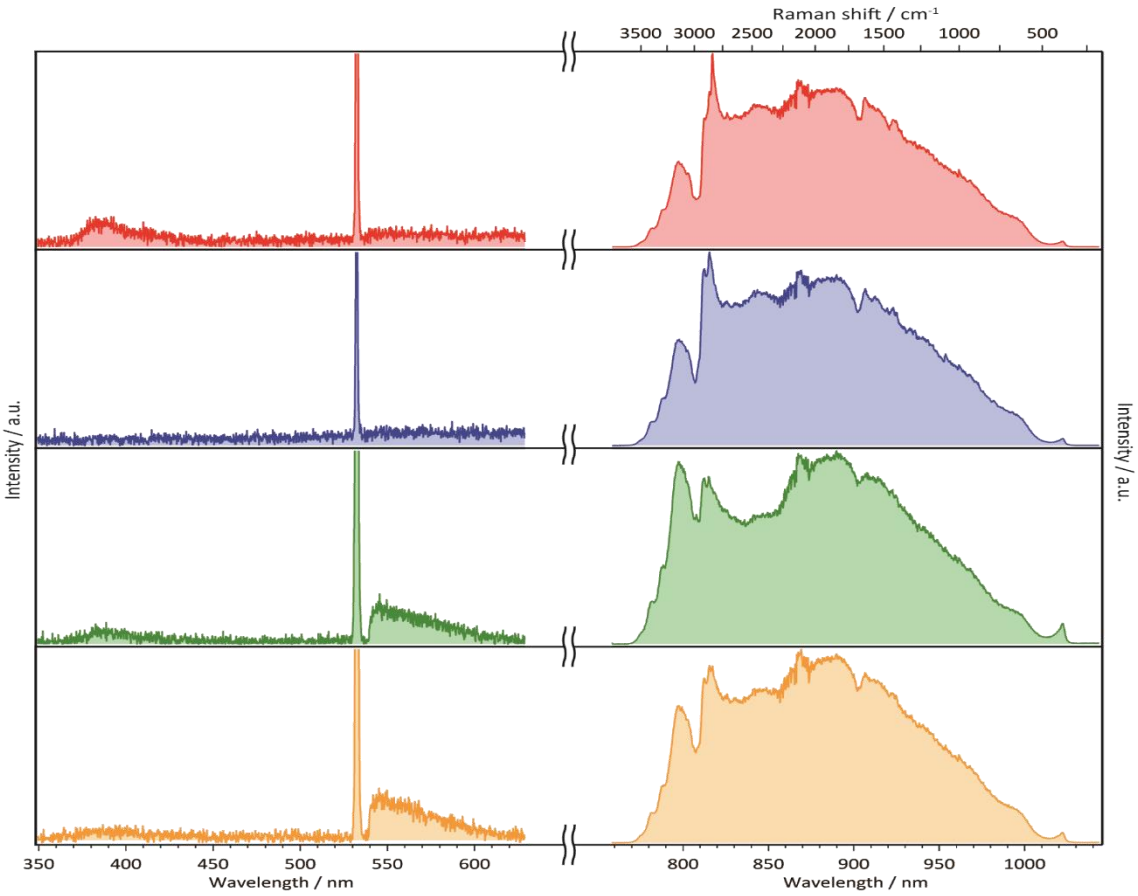

Fig. 4-2 Typical obtained spectra from the rat cornea sample. Differently colored spectra were obtained from different positions in the cornea.

The spectra shown in Fig. 4-3 are obtained Im[$\chi^{(3)}$] spectra after the application of MEM and noise removal by singular value decomposition analysis to the original spectra shown in Fig. 4-2[108]. The insets in each spectrum are expanded spectra around the fingerprint region (900 – 1800 cm^{-1}). Since the Im[$\chi^{(3)}$] spectra provide the same information as that the spontaneous Raman spectra provide, the assignment of the Raman band, which has been established by many previous studies, can be directly applied. Many molecular structural information is thus available from obtained Im[$\chi^{(3)}$] spectra. For example, the band at 1655 cm^{-1} is assigned to the superposition of the cis C=C stretch of lipids and the amide I mode of proteins. The band at 1446 cm^{-1} is assigned to the CH bend mode of methylene (CH_2) and methyl (CH_3) functional groups. The sharp band at 1003 cm^{-1} is assigned to the phenylalanine residues in proteins. The weak band at 1480 cm^{-1}, clearly recognizable in the blue spectrum, is assigned as the purine ring stretch mode. This mode can be used as a marker band for purine bases such as adenine and guanine in nucleotide. In the blue spectrum, the strong 1096 cm^{-1} band, corresponding to PO^{2-} stretch of phosphate group, is recognizable. This band can be used as the marker band of nucleic acid.

As shown in this section, by the extension of the TSFG microscope, multimodal detection of various nonlinear optical processes from the biological tissue sample was achieved. This multimodality makes the present method a powerful analytical tool for bioimaging. In the next section, I describe what can be visualized by TSFG and the other nonlinear processes in the rat cornea.

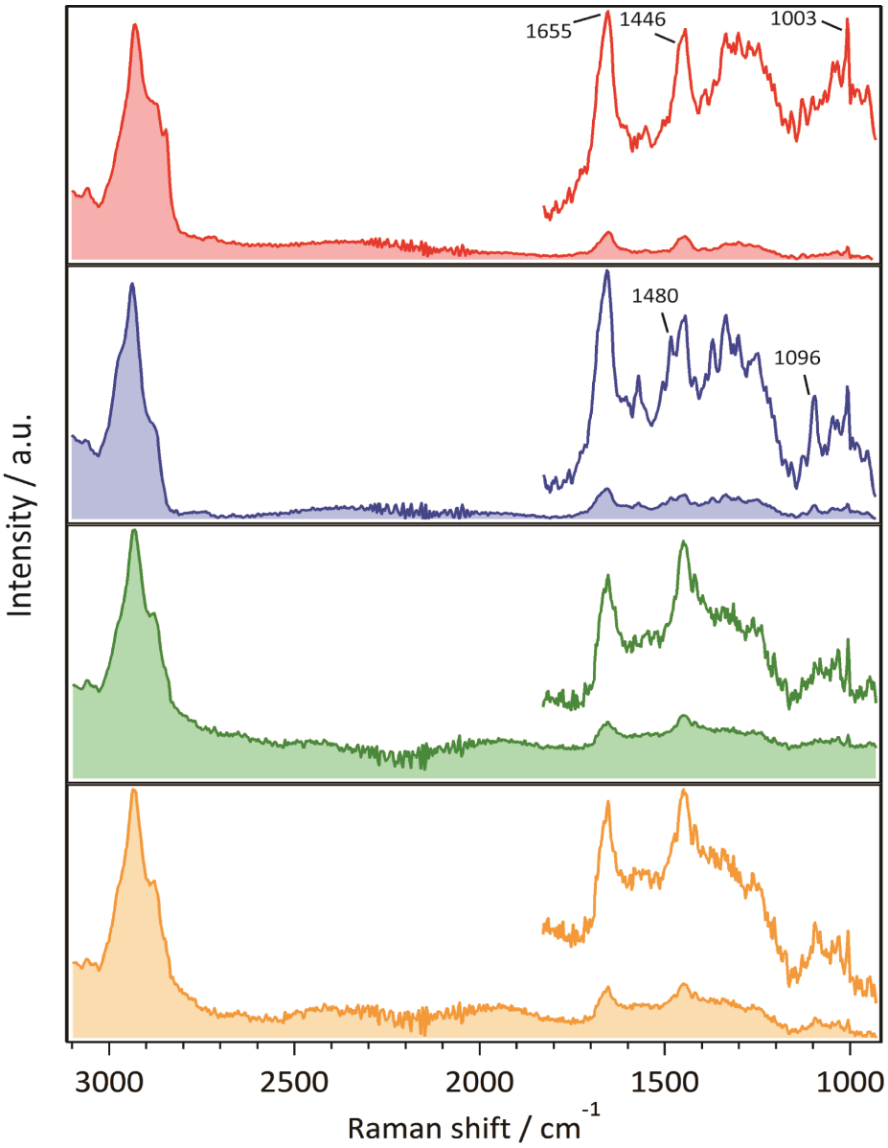

Fig. 4-3 Retrieved Im[$\chi^{(3)}$] spectra from those shown in Fig. 4-2. The insets correspond to the expansion of the fingerprint region spectra (900-1800 cm^{-1}).

4.4. Imaging of rat cornea

The rat cornea sample soaked in normal saline was observed by the developed setup. The abstract of the rat eye tissue is depicted in Fig. 4-4 and that of the rat cornea is shown in Fig. 4-5. Cornea locates at the most outside of the eye, which functions as the protection of the eye tissue. Although the cornea is apparently transparent, it possesses the complicated layered structure as shown in Fig. 4-5. The outer layer of the cornea is called corneal epithelium (Ep), which is composed of layered epithelial cells. The downside of the Ep is corneal stromal layer (St), whose main constituent is the type-I collagen fibers. St also contains keratocyte, kind of a fibroblast. The inner layer of the cornea is called corneal endothelium, which has monolayer endothelial cells. Between Ep and St, a membrane structure called Bowman's layer exists. On the other hand, a membrane like structure locates between St and endothelium is called Descemet's layer. It should be noted that this layered structure of the rat cornea cannot be visualized without pretreatment such as staining.

The images shown in Fig. 4-6 are depth direction images of the cornea observed by the developed optical system. Each image corresponds to (a) TSFG, (b) SHG, (c) CARS at CH_3 stretch, (d) CARS at CH_2 stretch, (e) CARS at CH bend, (f) CARS at purine ring stretch, and (g) CARS at phenylalanine residues, respectively. For reference, the H&E stained image of the cornea is also shown. It should be denoted that the sample of H&E staining was a frozen corneal section which was different sample from that nonlinear optical images (a)-(g) were observed. In these figures, the top part corresponded to Ep and the bottom is St. The scanning area of the image was 25 μm in the in-plane direction, and 175 μm in the depth direction. The available range of the image was restricted by the motion range of the piezo stage. Each image in Fig.4-6 provided the different images which is originated from the different contrast mechanism of each nonlinear optical process.

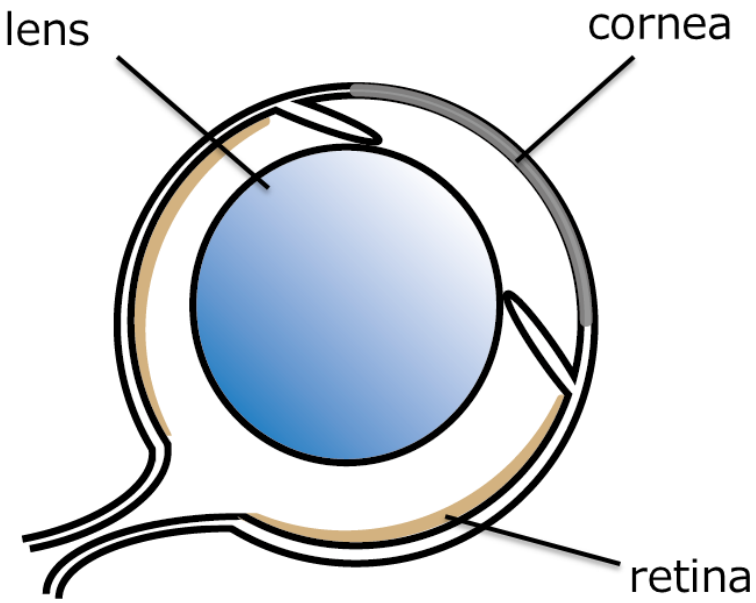

Fig. 4-4　Schematic of the rat eye tissue.

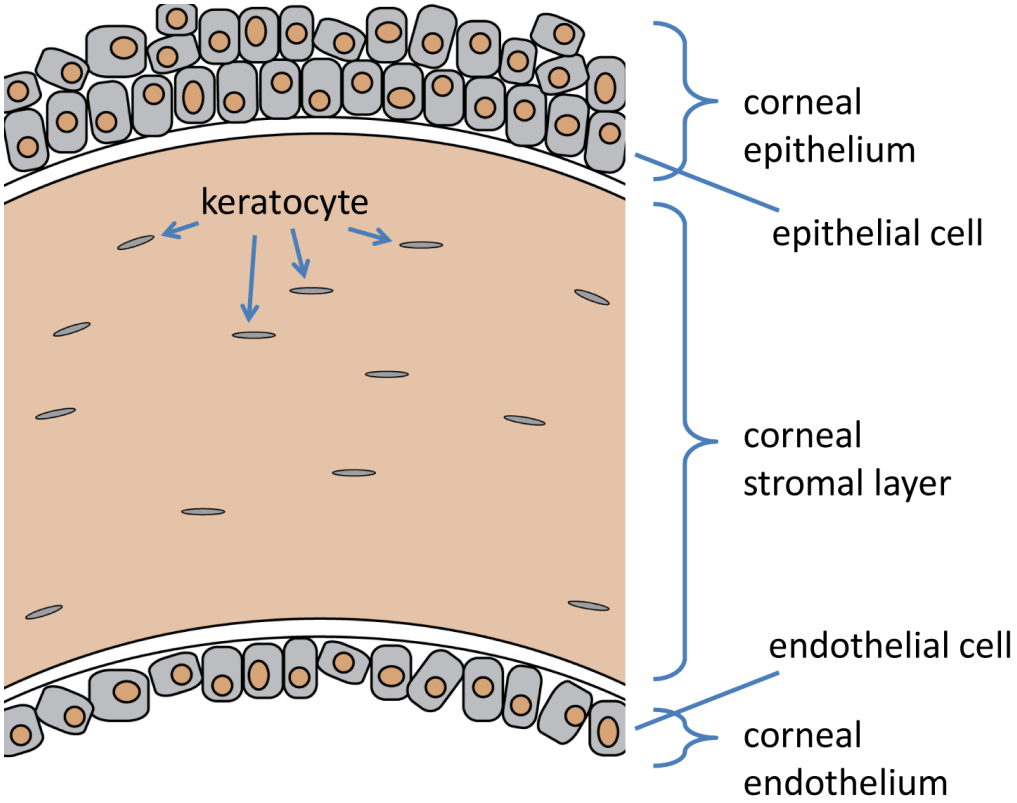

Fig. 4-5　Schematic of the rat cornea tissue.

In the TSFG image (Fig. 4-6a), the inside of the epithelial cells was visualized in Ep. This indicates that the intracellular structure of the epithelial cells is totally inhomogeneous. Between Ep and St, the membrane-like structure was visualized by TSFG. From the histological point of view, this structure is speculated as the basement membrane, which plays as a scaffold for epithelial cells. It is noteworthy that this structure was visualized only by TSFG. In St region, the flat structure was visualized.

In the SHG image (Fig. 4-6b), strong SHG signals were obtained from St layer. This result is consistent with the fact that the major component of St is type-I collagen fibers, which is known as a source of strong SHG signals[97,98]. In the CARS images (Fig. 4-6c-g), various structures were visualized based on the molecular structure of each layer. For example, in the CH_2 stretch image (Fig. 4-6d), the cell membrane of the epithelial cells were visualized (the image showed doughnut-shape in Ep) because lipid molecules, which is a major component of the cell membrane, contain a lot of CH_2 group. On the other hand, the purine ring image (Fig. 4-6f) visualized the nuclei of the epithelial cells (the inside of the cell showed the strong signals). Since nucleotide including adenine and guanine as a part of the constituent molecules of DNA and RNA, the nuclei can be visualized by the purine ring image. It is notable that all TSFG and CARS images showed the flat structure in St layer. This structure was thus speculated as keratocyte because all signals from proteins, lipids and nucleic acids were detected. Since the keratocyte was strongly pressed by the collagen fibers in the healthy cornea, the keratocyte could be regarded as the optically heterogeneous structure in St, which is filled with collagen fibers. Thus the signal of TSFG was detected.

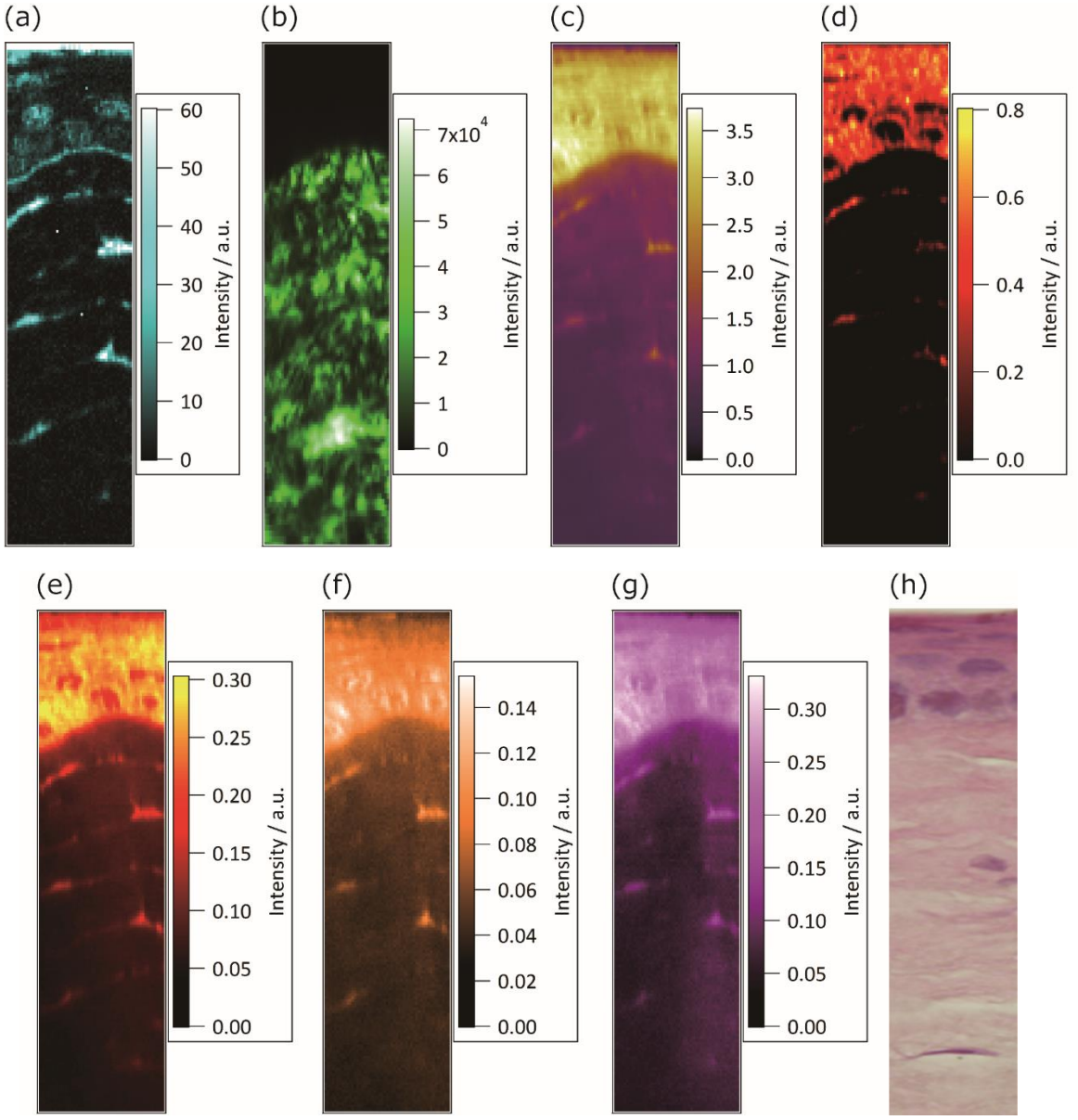

Fig. 4-6 Observed images of rat cornea in the depth direction. The scanning are is 25 μm in the in-plane direction, and 175 μm in the depth direction. (a) TSFG, (b) SHG, (c) CARS at CH_3 stretch, (d) CARS at CH_2 stretch, (e) CARS at CH bend, (f) CARS at purine-ring stretch, (g) CARS at phenylalanine residues, (h) referential H&E stained image.

The images shown in Fig. 4-7 and Fig. 4-8 are the in-plane direction images observed in Ep (Fig. 4-7) and St (Fig. 4-8). The scanning area was 100 μm x 100 μm. Each image corresponds to (a) TSFG, (b) SHG, (c) CARS at CH_3 stretch, (d) CARS at CH_2 stretch, (e) CARS at CH bend, (f) CARS at purine ring stretch, and (g) CARS at phenylalanine residues, respectively. Comparing Fig. 4-7 and Fig 4-8, it is clear that Ep and St possess totally different inner structures. In Ep layer (Fig. 4-7), cellular structures (cell membrane and nuclei) were clearly visualized by CARS images (Fig. 4-7d, f). In the TSFG image, the heterogeneous intranuclear structures were visualized. It is notable that the TSFG image of Ep cells is not completely overlapped with that of the CARS images by purine ring (nucleic acid). This means that the inner structure of nuclei of epithelial cells cannot be regarded as homogeneous. In addition, particle-like structures were also visualized by TSFG. This pattern was not observed in the other images. Presently, I speculate that the origin of the particle pattern is water, which is possibly becomes a source of TSFG but does not provide any significant spectral signatures of $\mathrm{Im}[\chi^{(3)}]$under the current condition. In St layer (Fig. 4-8), keratocyte was visualized in TSFG and CARS images (Fig. 4-8a, c-g). It is notable that SHG image (Fig. 4-8b) provided different patterns in comparison to the other images. Many fibrous structures in SHG image was speculated as the type-I collagen fibers. There are many types of collagens possessing different higher-order structures. For example, type-IV collagens is not filamentous but net-like structures. No SHG signal is thus detectable from type-IV collagens. Interestingly, the main constituent of the basement membrane which was mentioned in the axial direction image by TSFG (Fig. 4-6a) is type-IV collagens. It is thus reasonable that the membrane-like structure was not observed in the SHG image (Fig. 4-6b).

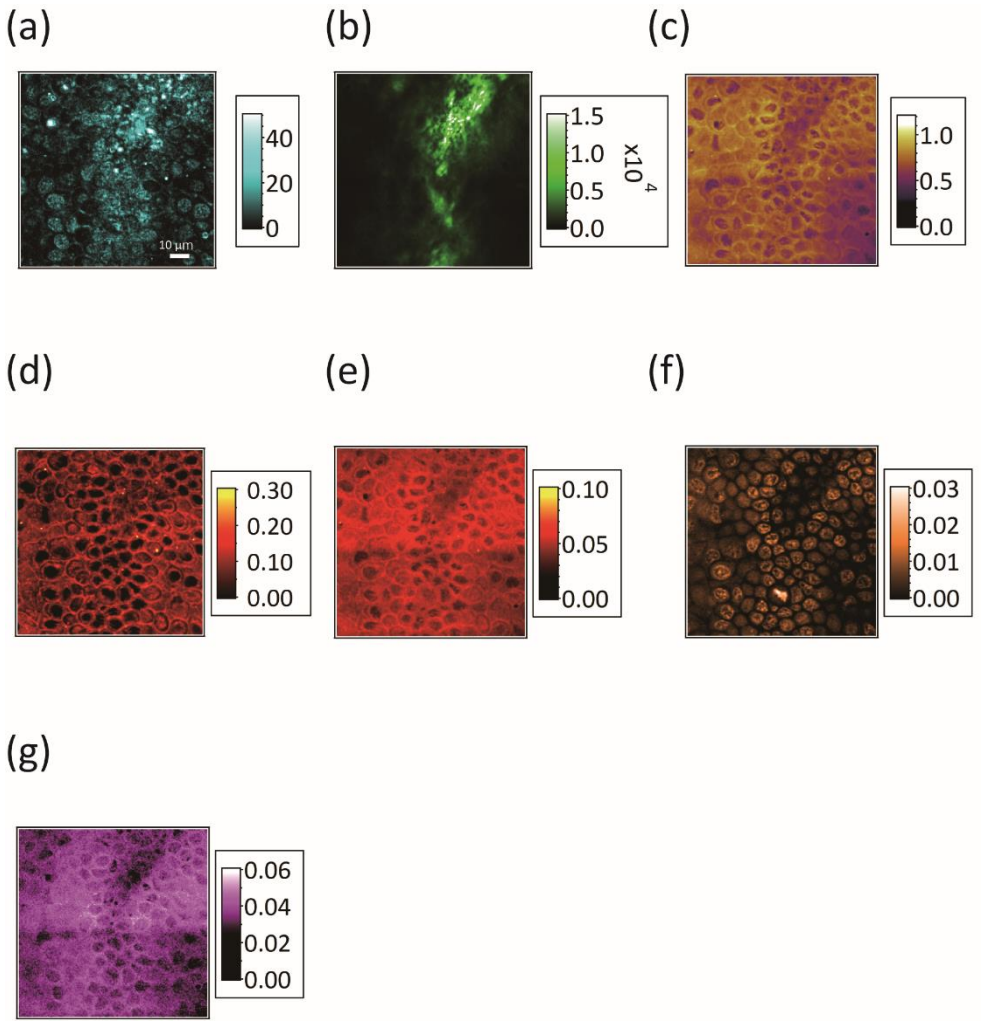

Fig. 4-7 Observed images of corneal Ep in the in-plane direction. (a) TSFG, (b) SHG, (c) CARS at CH_3 stretch, (d) CARS at CH_2 stretch, (e) CARS at CH bend, (f) CARS at purine-ring stretch, (g) CARS at phenylalanine residues. The image corresponds to 100 × 100 μm^2.

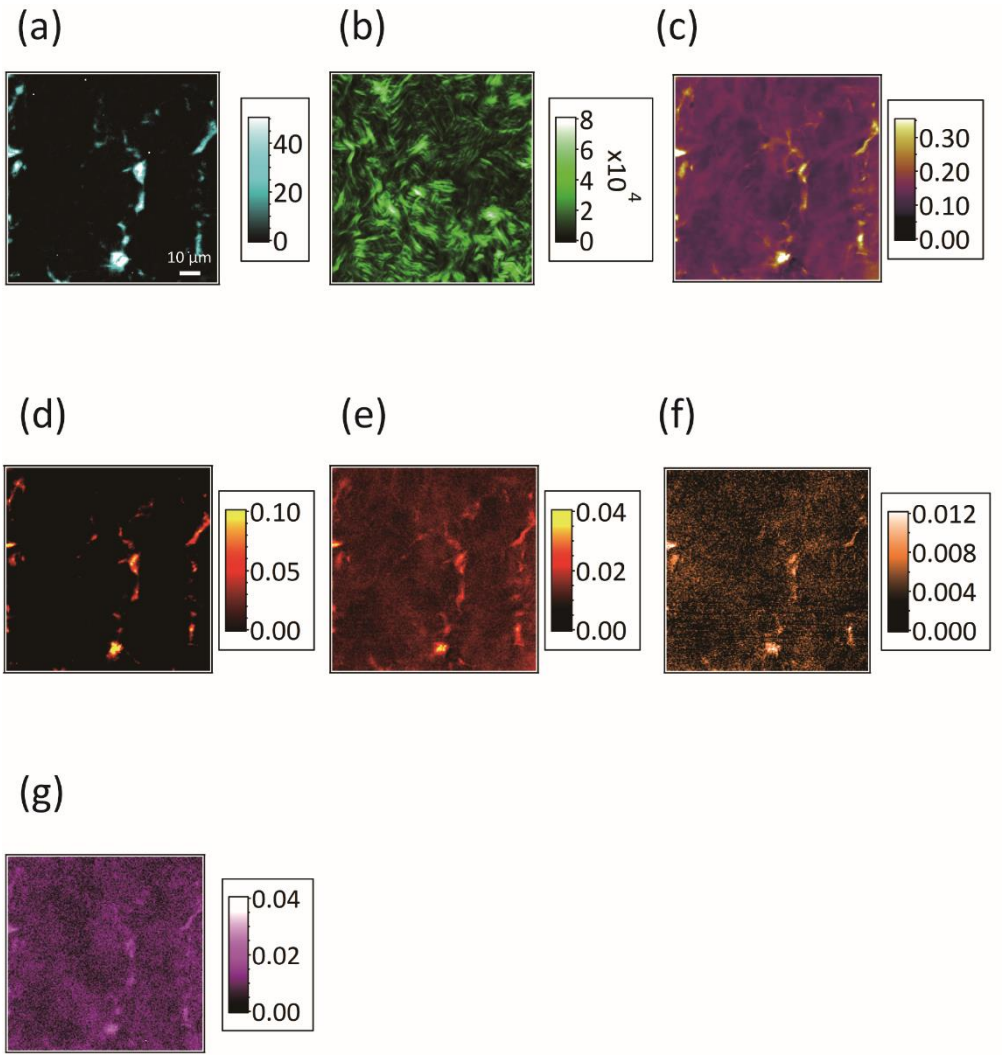

Fig. 4-8 Observed images of corneal St in the in-plane direction. (a) TSFG, (b) SHG, (c) CARS at CH_3 stretch, (d) CARS at CH_2 stretch, (e) CARS at CH bend, (f) CARS at purine-ring stretch, (g) CARS at phenylalanine residues. The image corresponds to 100 × 100 μm^2.

At last I performed three-dimensional imaging of the rat cornea *ex vivo*. Total 21 in-plane direction images (40 × 40 μm^2) were obtained with each 7.5 μm depth difference. Some of 21-depth resolved images, namely, 5 images with equidistant 22.5 μm depth positions from Ep (top) to St (bottom) are shown in Fig. 4-9. Since the optical axis of cornea tissue depends on the position of the sample, the optical axis of the microscopic system was different from that of the cornea. In Fig. 4-9, the left below part of the tissue was closer to the cover glass than the upper right. From the position of Ep to that of St, TSFG, SHG and CARS images showed characteristic depth dependence on their unique contrast mechanisms and their chemical specificities. In particular, doughnut-like and spot-like patterns are observed at the center and the edge of corneal epithelium by TSFG images. These patterns probably detect the boundary of nuclei in three-dimensional view.

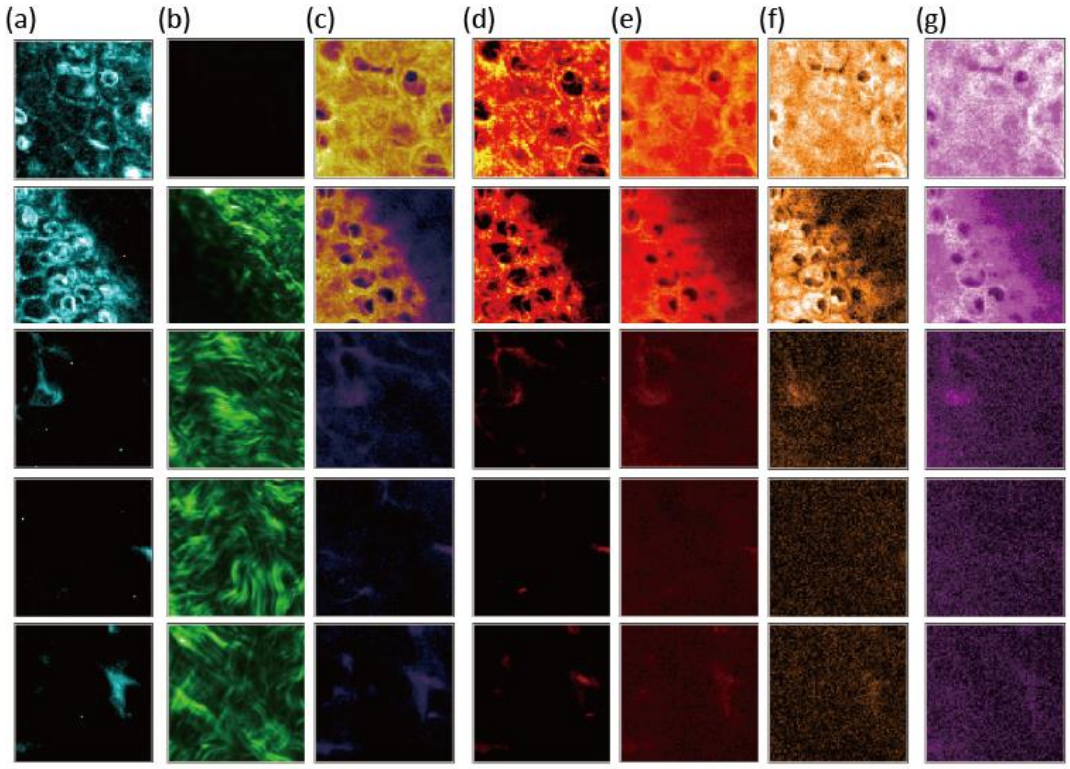

Fig. 4-9 Observed images of the rat cornea tissue in the three-dimensional direction; (a) TSFG, (b) SHG, (c) CARS at CH_3 stretch, (d) CARS at CH_2 stretch, (e) CARS at CH bend, (f) CARS at purine-ring stretch and (g) CARS at phenylalanine residues. The image corresponds to 40 × 40 μm^2.

4.5. Difficulty of the spectral analysis of TSFG from the tissue sample

In this chapter, I introduced the application of TSFG (and the other nonlinear optical processes) to the imaging of biological tissue samples. Obtained TSFG images provided characteristic pattern originated from the distinguishing contrast mechanism described in the previous chapter. Similar to the Hb experiment, it is expected that the detailed spectral analysis of TSFG provide the information on the molecular electronic state.

I tried to apply the spectral analysis established in the chapter 3 to the spectra obtained from the cornea. However, obtained spectral shapes were different from the Hb experiment. Especially, the spectral shape of TSFG signals showed the axial position dependence. Due to the positional dependence of TSFG, background of the TSFG spectra were unstable and the fitting with the Eq. 4 could not be applied. The reason of the depth position dependence is inferred to be the aberration caused by the thickness and the complicated structure of the corneal sample. Since the theory established in the chapter 3 supposes the aberration-free system, it is reasonable that the conclusion of the theory cannot be directly applied to the imaging of the cornea. In order to perform the correct spectral analysis, it is important to solve the positional dependence problem.

By the further development of the theory of TSFG and the optical system, it is expected that the difficulty of the spectral analysis of the multiplex TSFG will be overcome. This will enable the analysis of the electronic state (and the redox state) of the molecules inside the cornea. The development of the optical system will also enables various application. For example, real-time tracing of the wound healing process of the eye can be realized by the continuous measurement of TSFG, SHG and CARS signals.

4.6. **Short summary and future prospect**

In this chapter, the application of TSFG microspectroscopy to the observation of the biological tissue sample, rat cornea, was introduced. By the multimodality of nonlinear optical processes and extension of the optical system, simultaneous signal detection of TSFG, SHG and CARS was achieved. Since each nonlinear optical process is based on the unique contrast mechanism, the simultaneous detection makes the detailed molecular structural information inside the biological samples more accessible.

The application to the imaging of rat cornea revealed that the many intratissue and intracellular structures could be visualized through the multimodal imaging. In SHG image, the type-I collagen fiber generated the strong SHG signal and its oriented structure was visualized. In constructing CARS images, the application of MEM made the CARS spectra more informative. Resulted CARS images visualized the cellular membrane, nuclei and the distribution of the keratocyte. In TSFG images, some structures which were not visualized in the other imaging techniques could be found. The intranuclear structure given by TSFG indicates the heterogeneous environment of the nuclei. The speckle pattern which was currently speculated as water was visualized in Ep. The keratocyte was also visualized due to their flattened structure in St. Between Ep and St, the membrane structure speculated as the basement membrane was visualized, which was difficult to be observed by other analytical techniques. It should be emphasized that the current method enables the visualization of the detailed intrastructure of the cornea without any pretreatments.

In this thesis study, it was unsuccessful to elicit the molecular structural information from the spectral analysis of TSFG. This is presumably due to the optical aberration originated from the thickness of the corneal samples. Further development of the theory for the spectral analysis and the optical system will overcome the problem. This will make TSFG microspectroscopy more powerful analytical method to analyze the molecular electronic state in the tissue sample.

Chapter 5

Concluding remarks

In this thesis, I developed novel spectroscopic techniques which enabled analyzing the redox state of hemoproteins in the biological samples. To date, there have been many studies that reported the analytical methods to qualitatively or quantitatively analyze the redox state of hemoproteins. However, most of previously reported methods require the destructive experimental processes. The purpose of this thesis study is thus the development of the nondestructive analytical techniques of the redox state of hemoproteins.

In the chapter 2, I introduced the development of the 405 nm excitation resonance Raman microspectroscopy. Hemoproteins possess two major absorption bands, Q-band around 550 nm and Soret band around 410 nm. The 405 nm excitation RRS uses the resonance between the incident light and Soret band transition, which showed five times larger absorption coefficient than that of Q-band transition. As expected from the difference of absorption coefficients, 405 nm excitation scheme provided the stronger intensity of signals than those of previously reported 532 nm excitation scheme. By the combination with 405 nm excitation scheme and the spectral fitting technique, sensitive and detailed analysis of the redox state of cytochrome species was achieved. The developed setup was applied to trace the redox state dynamics of the intracellular cytochrome species during apoptosis. Although cyt b did not show any significant changes of the redox state, cyt c showed the drastic decrease of the reduced form. From the thermodynamic point of view, reduced cyt c is more inert than reduced cyt b to oxidation. These facts indicate that the oxidation of cyt c during apoptosis is performed through the target specific manner. This is the unique result achieved by the developed analytical method due to its nondestructivity and single cell level resolution. The previously reported techniques were not applicable to single cell analysis. This is the first study that reported the intracellular redox state dynamics during the signal transduction process.

In the chapter 3, I introduced electronically resonant TSFG microspectroscopy. Electronic resonance enhancement of TSFG signal was confirmed by the measurement of the hemoprotein solutions. In order to interpret the TSFG spectra, the signal generation mechanism

of TSFG was theoretically analyzed. It was revealed that the spectral distortion of multiplex TSFG spectra was originated from the relative phase difference of π between the resonant and the nonresonant terms of nonlinear susceptibility. Based on the theoretical analysis, obtained TSFG spectra were mathematically reconstructed. This result indicates that the redox state and the electronic state of Hb can be directly identified through the spectral analysis of the multiplex TSFG spectra. In general, UV-visible microspectroscopy was applied to analyze the molecular electronic state with the high spatial resolution. Compared with this technique, resonant TSFG microspectroscopy is considered to be more useful if the analyte was complicated samples such as the blood. Though UV-visible absorption is severely affected by the matrix effect, TSFG will overcome this problem due to its interface-sensitivity. Therefore resonant TSFG microspectroscopy offers rapid and robust analysis of the hemoproteins.

In the chapter 4, the application of TSFG microspectroscopy to the biological samples was described. The rat corneal tissue was observed by the developed microscope. In addition to TSFG, SHG and CARS signals were simultaneously detected. The inner structure of the rat cornea was visualized without any labeling. Each nonlinear optical processes provided the various information originated from the different contrast mechanism. Especially, TSFG visualized the inside of the epithelial cells, basement membrane and keratocyte. Though the multimodal imaging with TSFG provided the informative images, the detailed spectral analysis of TSFG which established in the chapter 3 was not applicable to the spectra obtained from the cornea. The aberration of the optical system induced by thick and complicated sample was inferred to be the reason of the failure of the spectral analysis. The modification of the aberration by the improvement of the optical setup and the establishment of the theory taking into account the aberration will enable the spectral analysis of TSFG obtained from the biological tissue samples.

In this thesis study, spectroscopic methods were applied to the analysis of the redox state of hemoproteins. Recently, there have been many studies that apply the spectroscopy to

biological samples and attempt to elucidate the relationship between the molecular structure and biological functions. However, it is generally difficult to obtain the significant information on the biological phenomena. This thesis study revealed that the redox state of hemoproteins could be identified by the spectroscopic method in a nondestructive manner. As introduced in the general introduction, the redox state of biomolecules including hemoproteins plays the important roles to maintain the life. At the present, the developed analytical techniques are applicable only for the targeted hemoproteins. There are many other redox active molecules, however, inside the life body including from small molecules such as flavin analog and nicotine analog, to large proteins. By tuning the excitation wavelength, the redox state of the redox active biomolecules other than hemoproteins might be analyzed through RRS or TSFG. And the development of the redox state analysis of biomolecules other than hemoproteins will elucidate the various novel relation between the redox state and life phenomena.

Acknowledgement

First of all, I would like to express my gratitude to Prof. Takeaki Ozawa, my supervisor in the Ph. D. course study. He arranged me the opportunity and environment to conduct the research using Raman spectroscopy and nonlinear optical spectroscopy. Without his support, I could not finish this thesis study.

I greatly appreciate to Dr. Rintaro Shimada. The enthusiastic discussion with him helped me a lot. I learned the basic and practice of spectroscopy, and the scientific thinking from him. I am also grateful to Dr. Hideaki Yoshimura. He taught me a lot about the biological aspect of the experiment. I am thankful to Dr. Masaki Takeuchi, Dr. Mitsuru Hattori and Dr. Liang-da Chiu for their daily maintenance of the laboratory.

I want to tell my great thank to all members of Ozawa Laboratory. The daily research life with them was delightful and fruitful. Especially, I thank Dr. Yusuke Nasu, Dr. Yoshihiro Katsura, Mr. Toshimichi Yamada, Mr. Mizuki Endo, Mr. Kazuki Fukuda, Ms. Qiaojing Li and Mr. Genki Kawamura.

I would like to tell my great gratitude to Prof. Hideaki Kano. I learned many things from his posture to science and research. He also gave me a lot of opportunities to have presentations of my research. Due to these presentations, I had a lot of fascinating experiences including discussion with sophisticated researchers all over the world.

I want to thank Prof. Hiro-o Hamaguchi and the previous members of Hamaguchi laboratory at the University of Tokyo. Though the members have already been separated, the conversation with them at the conference always stimulated me.

I also deeply thank many collaborators. Prof. Yuichi Kaji kindly provided me corneal samples and gave important suggestions about the rat cornea study. Dr. Naoki Fukutake taught me optics and nonlinear optics. The many part of the theoretical analysis of TSFG was

supported by him. In addition, he kindly gave me advice on my future career. I also appreciate to Prof. Philippe Leproux and Prof. Vincent Couderc. They provided me a white-light laser source and welcomed me on my first and second visiting to Limoges.

The members in national research institute of police science (NRIPS) also supported me. Especially, the members in First Chemistry Section in Third Department of Forensic Science generously helped me to finish the thesis. I deeply appreciated their kindness.

At last, I would like to express my gratitude to many people I met in my university life. The day I spent with them was my great motive power to continue this thesis study. I am also thankful to my family. Without them, I could not start and continue to go on my research life.

Bibliography

[1] C. H. Foyer, G. Noctor, *Plant Cell* **2005**, *17*, 1866–1875.

[2] P. D. Ray, B.-W. Huang, Y. Tsuji, *Cell. Signal.* **2012**, *24*, 981–990.

[3] D. Trachootham, W. Lu, M. A. Ogasawara, R.-D. V. Nilsa, P. Huang, *Antioxid. Redox Signal.* **2008**, *10*, 1343–1374.

[4] V. Borutaite, G. C. Brown, *J. Biol. Chem.* **2007**, *282*, 31124–31130.

[5] J. L. Martindale, N. J. Holbrook, *J. Cell. Physiol.* **2002**, *192*, 1–15.

[6] N. R. Madamanchi, A. Vendrov, M. S. Runge, *Arterioscler. Thromb. Vasc. Biol.* **2005**, *25*, 29–38.

[7] S. Leutner, A. Eckert, W. E. Müller, *J. Neural Transm.* **2001**, *108*, 955–967.

[8] B. S. Berlett, E. R. Stadtman, *J. Biol. Chem.* **1997**, *272*, 20313–20316.

[9] M. Paoli, J. Marles-Wright, A. Smith, *DNA Cell Biol.* **2002**, *21*, 271–280.

[10] Y. Hatefi, *Annu. Rev. Biochem.* **1985**, *54*, 1015–1069.

[11] I. J. Holt, A. E. Harding, R. K. Petty, J. A. Morgan-Hughes, *Am. J. Hum. Genet.* **1990**, *46*, 428–433.

[12] L. A. Esposito, S. Melov, A. Panov, B. A. Cottrell, D. C. Wallace, *Proc. Natl. Acad. Sci.* **1999**, *96*, 4820–4825.

[13] G. H. Loew, D. L. Harris, *Chem. Rev.* **2000**, *100*, 407–420.

[14] S. Orrenius, V. Gogvadze, B. Zhivotovsky, *Annu. Rev. Pharmacol. Toxicol.* **2007**, *47*, 143–183.

[15] J. C. Goldstein, N. J. Waterhouse, P. Juin, G. I. Evan, D. R. Green, *Nat. Cell Biol.* **2000**, *2*, 156–162.

[16] K. Kuida, T. F. Haydar, C.-Y. Kuan, Y. Gu, C. Taya, H. Karasuyama, M. S.-S. Su, P. Rakic, R. A. Flavell, *Cell* **1998**, *94*, 325–337.

[17] K. T. Schomacker, O. Bangcharoenpaurpong, P. M. Champion, *J. Chem. Phys.* **1984**, *80*, 4701-4717.

[18] P. Li, D. Nijhawan, I. Budihardjo, S. M. Srinivasula, M. Ahmad, E. S. Alnemri, X. Wang, *Cell* **1997**, *91*, 479–489.

[19] M. B. Hampton, B. Zhivotovsky, A. F. Slater, D. H. Burgess, S. Orrenius, *Biochem. J.* **1998**, *329 (Pt 1*, 95–99.

[20] Christie Matwee, D. H. Betts, W. Allan King, *Zygote* **1999**, *8*, 57–68.

[21] J. T. Greenberg, A. Guo, D. F. Klessig, F. M. Ausubel, *Cell* **1994**, *77*, 551–563.

[22] William C. Earnshaw, Luis M. Martins, S. H. Kaufmann, *Annu. Rev. Biochem.* **1999**, *68*, 383–424.

[23] J. Chandra, A. Samali, S. Orrenius, *Free Radic. Biol. Med.* **2000**, *29*, 323–333.

[24] P. S. Brookes, Y. Yoon, J. L. Robotham, M. W. Anders, S.-S. Sheu, *Am. J. Physiol. Cell Physiol.* **2004**, *287*, C817–C833.

[25] G. C. Brown, V. Borutaite, *Biochim. Biophys. Acta* **2008**, *1777*, 877–881.

[26] Z. Pan, D. W. Voehringer, R. E. Meyn, *Cell Death Differ.* **1999**, *6*, 683–688.

[27] R. M. Kluck, S. J. Martin, B. M. Hoffman, J. S. Zhou, D. R. Green, D. D. Newmeyer, *EMBO J.* **1997**, *16*, 4639–4649.

[28] D. Suto, K. Sato, Y. Ohba, T. Yoshimura, J. Fujii, *Biochem. J.* **2005**, *392*, 399–406.

[29] O. Bodansky, *Pharmacol. Rev.* **1951**, *3*, 144–191.

[30] D. D. Van Slyke, A. Hiller, J. R. Weisiger, W. O. Cruz, *J. Biol. Chem.* **1946**, *166*, 121–148.

[31] R. Smith, R. E. Gosselin, *Toxicol. Appl. Pharmacol.* **1966**, *8*, 159–172.

[32] R. O. Wright, W. J. Lewander, A. D. Woolf, *Ann. Emerg. Med.* **1999**, *34*, 646–656.

[33] C. V. Raman, *Indian J. Phys.* **1928**, *2*, 387-398.

[34] C. V. Raman, K. S. Krishnan, *Nature*, **1928**, *121*, 501-502.

[35] Z. Movasaghi, S. Rehman, I. U. Rehman, *Appl. Spectrosc. Rev.* **2007**, *42*, 493–541.

[36] Y.-S. Huang, T. Karashima, M. Yamamoto, H. Hamaguchi, *Biochemistry* **2005**, *44*, 10009–10019.

[37] H. Wu, J. V Volponi, A. E. Oliver, A. N. Parikh, B. A. Simmons, S. Singh, *Proc. Natl. Acad. Sci. U. S. A.* **2011**, *108*, 3809–3814.

[38] G. J. Puppels, F. F. de Mul, C. Otto, J. Greve, M. Robert-Nicoud, D. J. Arndt-Jovin, T. M. Jovin, *Nature* **1990**, *347*, 301–303.

[39] T. J. Romer, J. F. . I. Brennan, M. Fitzmaurice, M. L. Feldstein, G. Deinum, J. L. Myles, J. R. Kramer, R. S. Lees, M. S. Feld, *Circulation* **1998**, *97*, 878–885.

[40] M. Marro, A. Taubes, A. Abernathy, S. Balint, B. Moreno, B. Sanchez-Dalmau, E. H. Martínez-Lapiscina, I. Amat-Roldan, D. Petrov, P. Villoslada, *J. Biophotonics* **2013**, *7*, 724-7234.

[41] B. Prescott, W. Steinmetz, G. J. Thomas, *Biopolymers* **1984**, *23*, 235–256.

[42] R. Cicchi, C. Matthäus, T. Meyer, A. Lattermann, B. Dietzek, B. R. Brehm, J. Popp, F. S. Pavone, *J. Biophotonics* **2014**, *7*, 135–143.

[43] B. B. Johnson, W. L. Peticolas, *Annu. Rev. Phys. Chem.* **1976**, *27*, 465–521.

[44] T. G. Spiro, P. Stein, *Annu. Rev. Phys. Chem.* **1977**, *28*, 501–521.

[45] M. Okada, N. I. Smith, A. F. Palonpon, H. Endo, S. Kawata, M. Sodeoka, K. Fujita, *Proc. Natl. Acad. Sci. U. S. A.* **2012**, *109*, 28–32.

[46] F. A. Tezcan, J. R. Winkler, H. B. Gray, *J. Am. Chem. Soc.* **1998**, *120*, 13383–13388.

[47] S. Hu, I. K. Morris, J. P. Singh, K. M. Smith, T. G. Spiro, *J. Am. Chem. Soc.* **1993**, *115*, 12446–12458.

[48] M. Kakita, V. Kaliaperumal, H. Hamaguchi, *J. Biophotonics* **2012**, *5*, 20–24.

[49] M. Kakita, M. Okuno, H. Hamaguchi, *J. Biophotonics* **2013**, *6*, 256–259.

[50] J. Pyrih, K. Harant, E. Martincová, R. Sutak, E. Lesuisse, I. Hrdý, J. Tachezy, *Eukaryot. Cell* **2014**, *13*, 231–239.

[51] B. F. Van Gelder, E. C. Slater, *Biochim. Biophys. Acta* **1962**, *58*, 593–595.

[52] S. Alam, J. Yee, M. Couture, S. J. Takayama, W.-H. Tseng, A. G. Mauk, S. Rafferty, *Metallomics* **2012**, *4*, 1255–1261.

[53] C. A. Lieber, A. Mahadevan-Jansen, *Appl. Spectrosc.* **2003**, *57*, 1363–1367.

[54] J. B. Ramsey, *J. R. Stat. Soc. Ser. B. Stat. Methodol.*, **1969**, *31*, 350-371.

[55] Y. H. Ong, M. Lim, Q. Liu, *Opt. Express* **2012**, *20*, 22158–22171.

[56] C. L. Zavaleta, B. R. Smith, I. Walton, W. Doering, G. Davis, B. Shojaei, M. J. Natan, S. S. Gambhir, *Proc. Natl. Acad. Sci. U. S. A.* **2009**, *106*, 13511–13516.

[57] B. R. Lutz, C. E. Dentinger, L. N. Nguyen, L. Sun, J. Zhang, A. N. Allen, S. Chan, B. S. Knudsen, *ACS Nano* **2008**, *2*, 2306–2314.

[58] Y. Fan, Z. Chen, H. Ai, *Anal. Chem.* **2015**, *87*, 2802–2810.

[59] H. Ostergaard, A. Henriksen, F. G. Hansen, J. R. Winther, *EMBO J.* **2001**, *20*, 5853–5862.

[60] H. Østergaard, C. Tachibana, J. R. Winther, *J. Cell Biol.* **2004**, *166*, 337–345.

[61] B. F. L. Rodkey, E. G. Ball, *J. Biol. Chem.* **1950**, *182*, 17–28.

[62] P. F. Urban, M. Klingenberg, *Eur. J. Biochem.* **1969**, *9*, 519–525.

[63] H. Segawa, N. Fukutake, P. Leproux, V. Couderc, T. Ozawa, H. Kano, *Opt. Express* **2014**, *22*, 10416–10429.

[64] H. Segawa, M. Okuno, H. Kano, P. Leproux, V. Couderc, H.-O. Hamaguchi, *Opt. Express* **2012**, *20*, 9551–7.

[65] C.-H. Yu, S.-P. Tai, C.-T. Kung, W.-J. Lee, Y.-F. Chan, H.-L. Liu, J.-Y. Lyu, C.-K. Sun, *Opt. Lett.* **2008**, *33*, 387–389.

[66] C.-F. Chang, C.-H. Yu, C.-K. Sun, *J. Biophotonics* **2010**, *3*, 678–685.

[67] G. Veres, S. Matsumoto, Y. Nabekawa, K. Midorikawa, *Appl. Phys. Lett.* **2002**, *81*, 3714–3716.

[68] A. Mathy, K. Ueberhofen, R. Schenk, H. Gregorius, R. Garay, K. Müllen, C. Bubeck, *Phys. Rev. B. Condens. Matter* **1996**, *53*, 4367–4376.

[69] G. O. Clay, A. C. Millard, C. B. Schaffer, J. Aus-der-Au, P. S. Tsai, J. a. Squier, D. Kleinfeld, *J. Opt. Soc. Am. B* **2006**, *23*, 932-50.

[70] R. D. Schaller, J. C. Johnson, R. J. Saykally, *Anal. Chem.* **2000**, *72*, 5361–5364.

[71] L. Gebicka, E. Banasiak, *Acta. Biochim. Pol.*, **2009**, *56*, 509-513.

[72] R. Benesch, R. E. Benesch, G. Macduff, *Science*, **1964**, *144*, 68–69.

[73] N. Fukutake, *J. Opt. Soc. Am. B* **2013**, *30*, 2665–2675.

[74] T. Wilson, C. J. R. Shepparu, K. Löschke, "*Theory and Practice of Scanning Optical Microscopy*," **1984**, London: Academic Press.

[75] S. Feng, H. G. Winful, *Opt. Lett.* **2001**, *26*, 485–487.

[76] J. Cheng, X. S. Xie, *J. Opt. Soc. Am. B* **2002**, *19*, 1604–1610.

[77] A. C. Allison, *Curr. Opin. Immunol.* **2009**, *21*, 499–505.

[78] R. Sharma, L. Yin, Y. Geng, W. H. Merigan, G. Palczewska, K. Palczewski, D. R. Williams, Jennifer J. Hunter, *Biomed. Opt. Express* **2013**, *4*, 1285–1293.

[79] N. Horton, K. Wang, D. Kobat, C. Clark, *Nat. Photonics* **2013**, *7*, 205–209.

[80] M. Savoldelli, M. Merano, D. Donate, O. Albert, V. Nuzzo, G. Mourou, J.-M. Legeais, K. Plamann, P. F. G. Rodríguez, *J. Biomed. Opt.* **2007**, *12*, 064032–1–064032–11.

[81] S.-Y. Chen, H.-C. Yu, C.-K. Sun, I.-J. Wang, *J. Biomed. Opt.* **2009**, *14*, 044012–1-044012–7.

[82] S.-W. Teng, H.-Y. Tan, J.-L. Peng, H.-H. Lin, K. H. Kim, W. Lo, Y. Sun, W.-C. Lin, S.-J. Lin, S.-H. Jee, et al., *Invest. Ophthalmol. Vis. Sci.* **2006**, *47*, 1216–1224.

[83] J. M. Bueno, E. J. Gualda, A. Giakoumaki, P. Pérez-Merino, S. Marcos, P. Artal, *Invest. Ophthalmol. Vis. Sci.* **2011**, *52*, 5325–5231.

[84] M. Han, G. Giese, J. F. Bille, *Opt. Express* **2005**, *13*, 5791–5797.

[85] A. T. Yeh, N. Nassif, A. Zoumi, B. J. Tromberg, *Opt. Lett.* **2002**, *27*, 2082–2084.

[86] P. Steven, M. Hovakimyan, R. F. Guthoff, G. Hüttmann, O. Stachs, *J. Cataract Refract. Surg.* **2010**, *36*, 2150–2159.

[87] V. Raghunathan, Y. Han, O. Korth, N.-H. Ge, E. O. Potma, *Opt. Lett.* **2011**, *36*, 3891–3893.

[88] J. P. Pezacki, J. a Blake, D. C. Danielson, D. C. Kennedy, R. K. Lyn, R. Singaravelu, *Nat. Chem. Biol.* **2011**, *7*, 137–145.

[89] C.-Y. Chung, J. Boik, E. O. Potma, *Annu. Rev. Phys. Chem.* **2013**, *64*, 77–99.

[90] C. L. Evans, X. S. Xie, *Annu. Rev. Anal. Chem.* **2008**, *1*, 883–909.

[91] C. W. Freudiger, W. Min, B. G. Saar, S. Lu, G. R. Holtom, C. He, J. C. Tsai, J. X. Kang, X. S. Xie, *Science (80-.).* **2008**, *322*, 1857–1861.

[92] Y. Ozeki, W. Umemura, Y. Otsuka, *Nat. Photonics* **2012**, *6*, 845–851.

[93] M. C. Wang, W. Min, C. W. Freudiger, G. Ruvkun, X. S. Xie, *Nat. Methods* **2011**, *8*, 135–138.

[94] S. H. Parekh, Y. J. Lee, K. a Aamer, M. T. Cicerone, *Biophys. J.* **2010**, *99*, 2695–704.

[95] S. Yue, M. N. Slipchenko, J.-X. Cheng, *Laser Photon. Rev.* **2011**, *5*, 496–512.

[96] E. E. Hoover, J. A. Squier, *Nat. Photonics* **2013**, *7*, 93–101.

[97] F. Aptel, N. Olivier, A. Deniset-Besseau, J.-M. Legeais, K. Plamann, M.-C. Scbanne-Klein, E. Beaurepaire, *Invest. Ophthalmol. Vis. Sci.* **2010**, *51*, 2459–2465.

[98] N. Olivier, F. Aptel, K. Plamann, M.-C. Schanne-Klein, E. Beaurepaire, *Opt. Express* **2010**, *18*, 5028–5040.

[99] P. J. Campagnola, A. C. Millard, M. Terasaki, P. E. Hoppe, C. J. Malone, W. A. Mohler, *Biophys. J.* **2002**, *82*, 493–508.

[100] P. J. Campagnola, L. M. Loew, *Nat. Biotechnol.* **2003**, *21*, 1356–1360.

[101] D. A. Dombeck, K. A. Kasischke, H. D. Vishwasrao, M. Ingelsson, B. T. Hyman, W. W. Webb, *Proc. Natl. Acad. Sci. U. S. A.* **2003**, *100*, 7081–7086.

[102] S. V. Plotnikov, A. C. Millard, P. J. Campagnola, W. A. Mohler, *Biophys. J.* **2006**, *90*, 693–703.

[103] C. Di Napoli, F. Masia, I. Pope, C. Otto, W. Langbein, P. Borri, *J. Biophotonics* **2014**, *7*, 68–76.

[104] E. M. Vartiainen, H. A. Rinia, M. Müller, M. Bonn, *Opt. Express* **2006**, *14*, 3622-3630.

[105] M. Okuno, H. Kano, P. Leproux, V. Couderc, J. P. R. Day, M. Bonn, H. Hamaguchi, *Angew. Chem. Int. Ed. Engl.* **2010**, *49*, 6773–6777.

[106] Y. Liu, Y. J. Lee, M. T. Cicerone, *Opt. Lett.* **2009**, *34*, 1363–1365.

[107] M. T. Cicerone, K. A. Aamer, Y. J. Lee, E. Vartiainen, *J. Raman Spectrosc.* **2012**, *43*, 637–643.

[108] H.-J. van Manen, Y. M. Kraan, D. Roos, C. Otto, *J. Phys. Chem. B* **2004**, *108*, 18762–18771.